

## RESEARCH ARTICLE

# A nonlocal three-dimensional turbulence parameterization (NLT<sub>3D</sub>) for numerical weather prediction models

V. Kuell<sup>1</sup> | A. Bott<sup>1</sup>

Institute for Geosciences, University of  
Bonn, Bonn, Germany

**Correspondence**

A. Bott, Institute for Geosciences,  
University of Bonn, D-53121 Bonn,  
Germany  
Email: a.bott@uni-bonn.de

**Funding information**

Deutsche Forschungsgemeinschaft,  
Grant/Award Number: Bo 998/18-1

**Abstract**

With increasing resolution of numerical weather prediction (NWP) models, classical subgrid-scale processes become increasingly resolved on the model grid. In particular, turbulence in the planetary boundary layer (PBL) is vertically already partially resolved in contemporary models. For classical local PBL schemes, resulting up-gradient heat transports cannot be treated correctly. Thus, nonlocal turbulence schemes have been developed in the past. As the horizontal grid sizes of NWP models become smaller than a few kilometers, the large turbulence eddies in the PBL will also start to become partially resolved in the horizontal direction. A very flexible way to formulate nonlocal turbulent exchange is the transilient matrix method, which is used here to develop a new turbulence parameterization. The resulting NLT<sub>3D</sub> scheme applies transilient mixing matrices to subgrid-scale transports in all three dimensions. We compare results of WRF real-case simulations including our scheme, a classical local turbulence scheme (MYNN), and an existing nonlocal one-dimensional scheme (ACM2) with observations from field campaigns over homogeneous terrain (CASES-99) and complex terrain (CAPTEX). Over homogeneous terrain, all three schemes similarly well capture the observed surface fluxes and radiosonde profiles, whereas over complex terrain more differences become obvious. During a tracer release experiment (CAPTEX) over the Appalachian mountain region, the mixing and vertical extent of the PBL turn out to be decisive to reproduce the observed advection speed of the tracer-marked air mass. Deeper mixing not only accelerates surface winds but also enables tracer to travel faster at higher altitudes and then mix back to the ground. As results from a version of NLT<sub>3D</sub> with only standard horizontal Smagorinsky diffusion (NLT<sub>1D</sub>) demonstrate, simulating three-dimensional turbulence can be beneficial already at horizontal grid sizes of a few kilometers.

**KEYWORDS**

boundary layer, dispersion, fraction skill score, small-scale modeling, tracer transport, transilient matrix, turbulence parameterization

## 1 | INTRODUCTION

During the first decades of numerical weather prediction (NWP), the Reynolds-averaged model equation system was usually closed by eddy-diffusivity schemes (the K approach) to represent turbulence in the planetary boundary layer (PBL) and above (e.g., Schmidt, 1925; Louis, 1979; Mellor and Yamada, 1982). The classical K approach considers only one-dimensional (1D) grid columns and an interaction between adjacent height levels when parameterizing turbulent fluxes, that is, the correlation terms of subgrid-scale fluctuations of the vertical wind  $w$  and any other conserved quantity  $\psi$  (heat, momentum, tracer species).

$$\overline{w'\psi'} = -K_z^\psi \frac{\partial \psi}{\partial z}. \quad (1)$$

Here, the eddy diffusivity  $K_z^\psi$  is a function of height, buoyancy, wind shear, etc. and has to be parameterized. Such schemes have later been classified as 1D local schemes.

When NWP models became spatially higher resolved and more sophisticated, a number of weaknesses of this approach became obvious, the most prominent being the problem of up-gradient transports of heat near the PBL top (e.g., Deardorff, 1966; Blackadar, 1979; Stull, 1984; Troen and Mahrt, 1986) or at the top of canopy layers (e.g., Inçan *et al.*, 1996; Ni, 1997; Foken, 2006). Such heat transports in the upward direction at local positive vertical gradients of the potential temperature  $\theta$  can be understood in terms of nonlocal heat transports by large eddies originating from warmer layers far below. These turbulent transports crossing several vertical model layers correspond to strong updrafts extending up to the whole PBL depth. To catch the structures of such big eddies, several modeling approaches have been proposed:

### 1. Extended K approaches:

By subtracting an additional term  $\gamma$  from the local gradient, turbulent fluxes were made positive in situations of nonlocal transports (e.g., Troen and Mahrt, 1986; Hong *et al.*, 2006).

$$\overline{w'\psi'} = -K_z^\psi \left( \frac{\partial \psi}{\partial z} - \gamma \right). \quad (2)$$

### 2. Eddy-diffusion mass flux (EDMF) schemes:

Originating from mass flux convection schemes, where updrafts (of deep cumulus convection) usually extend over a number of vertical levels, the idea of combining the mass flux approach for nonlocal transports (large eddies) and K approach for local transports (small eddies) was introduced (e.g., Teixeira and Siebesma, 2000;

Soares *et al.*, 2004):

$$\overline{w'\psi'} = -K_z^\psi \frac{\partial \psi}{\partial z} + M(\psi^{up} - \overline{\psi}). \quad (3)$$

Similar to convection schemes, here a vertical mass flux  $M$  has to be parameterized.

### 3. Transilient turbulence schemes:

Considering turbulent transports between all combinations of vertical source and target model levels  $k$  and  $l$ , a mixing matrix can be constructed. Stull (1984); Stull and Hasegawa (1984); Fiedler (1984); Fiedler and Moeng (1985); Stull and Driedonks (1987) coined the notion *transilient turbulence theory* for this approach. Discretized on a vertical grid with  $N_z$  layers (and layer indices  $k, l$ ), this approach can be written as

$$\psi_k(t_{n+1}) = \sum_{l=1}^{N_z} C_{k,l}(t_n, \Delta t) \psi_l(t_n). \quad (4)$$

Because of the very general and comprehensive character of the so-called transilient (mixing) matrix  $C$ , the actual challenge is to fill the matrix elements with physical contents. Several approaches to do so have been presented to date (see, e.g., Pleim and Chang, 1992; Stull, 1993; Pleim, 2007a; 2007b and references therein). The idea has even been transferred to the parameterization of deep cumulus convection (Forster and Stohl, 2007; Roms and Kuang, 2011).

The schemes summarized under categories 1–3 are classified as 1D nonlocal schemes. A very early three-dimensional (3D) turbulence parameterization, that is, including also horizontal wind correlation terms  $\overline{u'\psi'}$  and  $\overline{v'\psi'}$ , has already been introduced by Smagorinsky (1963). Although this scheme was originally developed for use in coarse-resolved global models, it is sophisticated enough to be still successfully applied in contemporary NWP models.

The further increase in computer power has facilitated decreasing spatial grid sizes. In particular, when entering the regime of grid spacings below 1 km for operational use in the near future, nonlocal 3D turbulence parameterization is demanded. Eddies extending vertically over the whole PBL (say  $\Delta z \approx 2$ –3 km for convective boundary layers) will soon also extend horizontally over several grid boxes rather than being confined to the local grid column. Raymond and Stull (1990) proposed an approach to extend a transilient turbulence scheme to three dimensions by introducing horizontal local eddy mixing between directly adjacent (vertically) turbulent grid boxes.

To avoid confusion in the notions of local and nonlocal, we define “local” as interactions between directly adjacent grid boxes only, irrespective of the vertical or horizontal

direction. “Nonlocal” then denotes interactions across several grid boxes in either the vertical or the horizontal direction. The classical schemes with the usual vertical K approach are then classified as vertically local schemes, that is, with interactions only between directly adjacent layers. They are also 1D, since there is no horizontal interaction at all.

As a comprehensive intercomparison campaign of NWP models and PBL schemes, the Global Energy and Water Exchanges (GEWEX) Atmospheric Boundary Layer Studies (GABLS) 1, 2, and 3 (Beare *et al.*, 2006; Cuxart *et al.*, 2006; Svensson *et al.*, 2011; Bosveld *et al.*, 2014) focusing on idealized as well as real cases (CASES field campaigns, LeMone *et al.*, 2000; Poulos *et al.*, 2002) were conducted. Svensson *et al.* (2011) state that, for testing a PBL scheme, embedding it in a NWP model is crucial (rather than an externally forced standalone test) due to the interaction with large-scale advection and the land-surface scheme. In the GABLS studies, PBL schemes tend to underestimate the surface sensible heat fluxes at daytime but overestimate their magnitude at nighttime. They also find that the PBL depth and profiles for convective cases are better simulated by vertically nonlocal PBL schemes. Holtslag *et al.* (2013) finds that PBL schemes are usually too active in stable PBL situations but that they also have to prevent a decoupling of the atmosphere from the ground resulting in runaway effects.

In this study, we present a new turbulence scheme that is by construction nonlocal in all three dimensions. In the vertical direction, not only adjacent layers interact by means of small eddies, but as far as physically justified by buoyancy and wind shear, also more distant layers can be mixed by relatively large eddies. In the horizontal direction, the new scheme will be capable of turbulent exchange between adjacent grid columns and will allow for horizontal nonlocal mixing. This will be accomplished by applying a transilient mixing matrix approach to all three dimensions. Although the horizontal mixing matrices are sparsely populated, thus limiting extensive computational costs, this approach allows for future extensions beyond directly adjacent grid columns when not only vertical but also horizontal grid sizes may be well below 1 km.

The present paper is organized in five sections: After introducing the hosting model for our simulations, we describe the development of the new NLT<sub>3D</sub> scheme (Section 2) and the observational data used to compare real case simulations with (Section 3). In Section 4, we employ the NLT<sub>3D</sub> scheme to simulate several real cases. Simulations over homogeneous terrain including comparisons with observed surface fluxes and radiosonde profiles are used to confirm the overall behavior of the scheme, to evaluate its performance under well-defined conditions and its independence of the chosen grid spacing (Section 4.1).

A tracer dispersion study is employed in Section 4.2 to evaluate the details and peculiarities of the NLT<sub>3D</sub> scheme by comparing it with existing turbulence schemes under more complex conditions, that is, over inhomogeneous terrain. The effects of including horizontal turbulence in the NLT<sub>3D</sub> scheme is analyzed for both simulation groups in Section 4.3. Finally, in Section 5, some conclusions of the study are presented.

## 2 | MODEL

### 2.1 | Hosting model

As the hosting model for our studies, we choose the Weather Research and Forecasting (WRF) model (version 4.1.4) with the Advanced Research WRF (ARW) dynamical core (Skamarock *et al.*, 2019). WRF is a fully compressible and nonhydrostatic mesoscale NWP model with advanced dynamics, physics, and numerics that is widely used for both research and operational purposes. The model solves the nonhydrostatic equations on an Arakawa C grid with terrain-following  $\eta$  vertical coordinates, that is, standard  $\sigma$  coordinates based on the dry hydrostatic pressure  $p_{hd}$  (Laprise, 1992). The prognostic variables are the three wind components  $u, v, w$ , the virtual potential temperature  $\theta_v$ , the total column pressure difference  $\mu = p_{\text{surf}} - p_{\text{top}}$ , the geopotential  $\phi$ , and a configuration-dependent set of specific contents of moisture species  $q_x$ .

The model is initialized and hourly provided with boundary data from the European Centre for Medium-Range Weather Forecasts (ECMWF) ERA5 reanalysis datasets (Hersbach *et al.*, 2020), which has a horizontal grid size of 0.25° (publicly accessible at <https://cds.climate.copernicus.eu>). We employ a stretched vertical grid with 60 layers and layer depths of 50 m near the ground and 350 m near the model top at 50 hPa (about 20 km).

Among the physical parameterization schemes available in WRF, we employ the Goddard long-wave and short-wave radiation schemes (Chou and Suarez, 1999; 2001), the Goddard microphysics scheme (Tao *et al.*, 1989; Tao *et al.*, 2016), the Noah surface (soil) model (Tewari *et al.*, 2004), and the revised Monin–Obukhov scheme for the surface layer (Jimenez *et al.*, 2012). To parameterize turbulence effects, we use the present NLT<sub>3D</sub> scheme and for comparison the ACM2 scheme (Pleim, 2007a; 2007b), which is a 1D vertically nonlocal scheme based on transilient turbulence theory, and the 1D vertically local MYNN scheme (Mellor and Yamada, 1982; Nakanishi and Niino, 2006; 2009; Olson *et al.*, 2019) based on eddy diffusion.

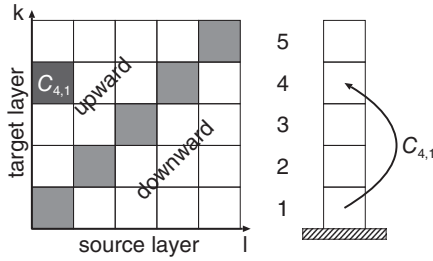


**FIGURE 1** Illustration of the transilient mixing matrix  $C$  and the effect of its elements in a discretized  $\psi$  profile. The element  $C_{4,1}$ , for example, denotes the mass specific portion of  $\psi$  transported from layer 1 to layer 4 in the local grid column. For more details see text

## 2.2 | The NLT<sub>3D</sub> scheme

Following the approach of transilient turbulence theory (e.g., Stull, 1984; 1993), the NLT<sub>3D</sub> scheme parameterizes a mixing matrix  $C$  to determine the grid-scale effect of turbulence for the vertical profile of a conserved prognostic variable  $\psi$  (e.g., virtual potential temperature  $\theta_v$ , specific moisture  $q_v$ , cloud water and ice  $q_c, q_i$ , and the horizontal wind components  $u, v$ ). Introducing the turbulent  $\psi$  tendency and  $\psi^n$  as a shortcut for  $\psi(t_n)$ , Equation 4 can be rewritten for the profile vector  $\psi^{n*}$  after the inclusion of turbulence effects.  $\psi_k^{n*}$ , denoting the value in the  $k$ th layer, is then given as

$$\psi_k^{n*} = \psi_k^n + \Delta t \left. \frac{\partial \psi_k^n}{\partial t} \right|_{turb} = \sum_{l=1}^{N_z} C_{k,l} \psi_l^n \quad (5)$$

The transilient matrix  $C$  depends on time, as turbulent activity may vary, and on the numerical time step  $\Delta t$ , as the same turbulent activity will change  $\psi^n$  more strongly after a longer time  $\Delta t$ .

Figure 1 sketches the effects of the single matrix elements on a  $\psi$  profile. Compared with the mathematical convention, the graphical matrix representation is vertically mirrored to make the assignment to upward and downward transports more suggestive. For an element  $C_{k,l}$ , the index  $l$  denotes the source layer and  $k$  the target layer. Obviously, for  $k > l$  (above diagonal) this is an upward transport, and for  $k < l$  (below diagonal) this is a downward transport. The farther the matrix element away from the diagonal, that is, the larger value of  $|k - l|$ , the longer the vertical distance bridged by the corresponding transport. The diagonal element  $C_{k,k}$  represents the portion of the substance or property  $\psi$  that remains in layer  $k$ .

### 2.2.1 | Transilient matrix

The main task now is to provide the transilient matrix  $C$  in Equation 5 with physically meaningful contents, that is,

the actual turbulence parameterization. As in Stull (1993), we split the atmosphere vertically into the PBL and the free atmosphere above. Throughout the PBL, both vertically nonlocal mixing and local mixing are assumed to occur and are parameterized in the same way. We choose an approach similar to Stull (1993), which makes use of the nonlocal Richardson number  $\tilde{Ri}_{k,l}$ :

$$\tilde{Ri}_{k,l} = \frac{2g}{\theta_{v,k} + \theta_{v,l}} \frac{(\theta_{v,k} - \theta_{v,l})(z_k - z_l)}{(u_k - u_l)^2 + (v_k - v_l)^2}. \quad (6)$$

To convert the nonlocal Richardson number into a measure for turbulent mixing, we follow Stull (1993) by introducing the turbulence efficiency as  $\eta_{turb} = (1 - \tilde{Ri}_{k,l}/Ri_T)$  with the terminal Richardson number  $Ri_T = 2$ . For the transilient matrix elements  $C_{k,l}$ , Stull (1993) obtains

$$C_{k,l} = \frac{1}{k_{PBL}} \underbrace{\frac{u_0 \Delta t}{|z_k - z_l|}}_{\gamma} \eta_{turb}(\tilde{Ri}_{k,l}). \quad (7)$$

We follow this approach except for two details: first, we construct an asymmetric scheme following the basic design of ACM2 (Pleim, 2007a; 2007b) with downdrafts not being formulated as mirrored updrafts. Thus, we limit Equation (7) to the updraft matrix elements  $C_{k,l}|_{k>l}$ . Second, in Stull (1993) the weighting factor  $\gamma$ , which can be interpreted as a portion of the convective overturning cycle during one time step  $\Delta t$ , assumes a fixed turbulent velocity of  $u_0 = 0.5 \text{ m}\cdot\text{s}^{-1}$ . We scale  $\eta_{turb}$  with the turbulent convective overturning time scale  $\Delta t_*$ , which can be estimated from the surface buoyancy flux  $w'\theta'_v|_{sfc}$  as

$$\Delta t_* = \frac{h_{PBL}}{w_*} \quad \text{with} \quad w_* = \sqrt[3]{h_{PBL} \frac{g}{\theta_{v,sfc}} \overline{w'\theta'_v|_{sfc}}} = u_* \sqrt[3]{\frac{h_{PBL}}{\kappa |L_*|}}. \quad (8)$$

Here,  $u_*$ ,  $\kappa = 0.40$ , and  $L_*$  are, respectively, the friction velocity, the von Kármán constant, and the Obukhov length. The relation of these quantities to the vertical velocity scale  $w_*$  can be found in Stull (1988). The PBL depth  $h_{PBL}$  is determined as function of the bulk Richardson number criterion following Pleim (2007a). Within a time step  $\Delta t$ , a well-established large-scale eddy will turn over by a fraction  $\Delta t/\Delta t_*$ . Hence, different from Stull (1993) (cf. Equation 7), we write for the updraft elements of the matrix  $C$ :

$$C_{k,l}|_{k>l} = \frac{1}{2} \frac{1}{k_{PBL}} \underbrace{\frac{\Delta t}{\Delta t_*} \frac{h_{PBL}}{|z_k - z_l|}}_{\gamma} \underbrace{\left(1 - \frac{\tilde{Ri}_{k,l}}{Ri_T}\right)}_{\eta_{turb}} \quad (9)$$



Although the scaling factor  $1/k_{\text{PBL}}$  adopted from Stull (1993) has been introduced for an equidistant vertical grid and vertically constant density throughout the PBL, here we maintain it in the more general framework for two reasons. First, we see the necessity for such a factor, which yields unity if summed up over all layers in the PBL, only for normalization and limitation of the matrix elements. Second, an apparently more attractive mass-weighting prefactor would otherwise lead to problems: if mass weighting is applied with respect to the source layer mass, this mass is considered twice, which results in quadratic dependence of the transported air mass from the source layer mass. On the other hand, if mass weighting is applied with respect to the target layer mass, it is either unphysical that the rising air mass should depend on the mass that will be encountered in the target layer or possible excess mass has to be postponed for deposition in a higher/lower layer. This, however, could contradict the target altitude already derived from the Richardson number stability criterion (Equation 6). Similar to Stull (1993), the last term in parentheses is limited to  $[0, 1]$ .

In the free atmosphere, we reduce turbulent activity to local mixing only. Following classical local turbulence theory with small eddies, from Equation (4) we obtain

$$\psi_k^{n+1} = C_{k,k-1}\psi_{k-1}^n + C_{k,k}\psi_k^n + C_{k,k+1}\psi_{k+1}^n, \quad (10)$$

involving only the directly adjacent model layers above and below the local layer. Conservation of mass and of the quantity  $\psi$  requires that, for  $N_z$  vertical layers (cf. Stull, 1993):

$$\sum_{l=1}^{N_z} C_{k,l} = 1 \quad \text{for all } k \quad \text{and} \quad \sum_{k=1}^{N_z} \frac{m_k}{m_l} C_{k,l} = 1 \quad \text{for all } l. \quad (11)$$

Here,  $m_k = \Delta z_k \rho_k$  is the mass column density of the  $k$ th grid box in the vertical. This determines  $C_{k,k} = 1 - C_{k,k-1} - C_{k,k+1}$ , which yields together with Equation 10

$$\psi_k^{n+1} - \psi_k^n = C_{k,k-1}(\psi_{k-1}^n - \psi_k^n) + C_{k,k+1}(\psi_{k+1}^n - \psi_k^n). \quad (12)$$

Local mixing by turbulent eddies is allowed throughout the whole atmosphere. To express this in terms of the mixing matrix formalism, classical eddy coefficients  $K$  have to be related to the transilient matrix elements. We start with the continuity equation for the conserved quantity  $\psi$  with diffusion fluxes set to zero:

$$\frac{\partial(\rho\psi)}{\partial t} + \nabla \cdot (\rho \mathbf{v} \psi) = S_\psi \quad (13)$$

Now we apply the usual Reynolds averaging ( $a = \bar{a} + a'$ ) and Hesselberg averaging, which is a density

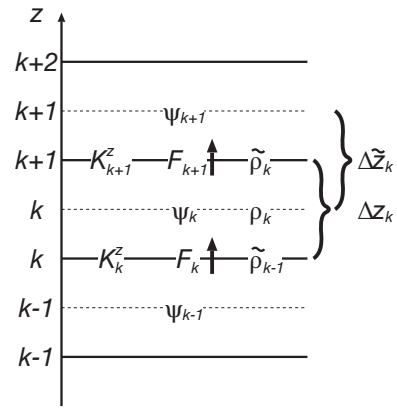


**FIGURE 2** Discretization of quantities relevant to turbulence on the vertical grid in WRF. Layer boundaries are drawn as solid lines, and layer (mass) centers are represented by dashed lines

( $\rho$ )-weighted Reynolds averaging ( $a = \hat{a} + a''$  with  $\hat{a} = \overline{a\rho}/\bar{\rho}$ ). Using the continuity equation of total mass, this results in (cf., e.g., Zdunkowski and Bott, 2003):

$$\frac{\partial \hat{\psi}}{\partial t} = -\frac{1}{\bar{\rho}} \hat{\mathbf{v}} \cdot \nabla \hat{\psi} - \underbrace{\frac{1}{\bar{\rho}} \nabla \cdot (\bar{\rho} \mathbf{v}'' \psi'')}_{\left. \frac{\partial \psi}{\partial t} \right|_{\text{turb}}} + \frac{\bar{S}_\psi}{\bar{\rho}}. \quad (14)$$

Preliminarily, we only consider the vertical component of the turbulent flux divergence. For the sake of simplicity, from now on we omit the averaging symbols (except for the correlation terms). The eddy diffusion flux  $F^\psi$  produces a turbulent  $\psi$  tendency of

$$\left. \frac{\partial \psi}{\partial t} \right|_{\text{turb}} = -\frac{1}{\rho} \frac{\partial F^\psi}{\partial z} \quad \text{with} \quad F^\psi = \rho \overline{w'' \psi''} = -\rho K^z \frac{\partial \psi}{\partial z}. \quad (15)$$

Discretization of this equation on the vertical grid of WRF (cf. Figure 2) and subsequent expression of the turbulent tendency by means of Equation (12) results in

$$\begin{aligned} -\frac{1}{\rho_k} \frac{F_{k+1} - F_k}{\Delta z_k} &= \frac{\psi_k^{n+1} - \psi_k^n}{\Delta t} \\ &= \frac{C_{k,k-1}(\psi_{k-1}^n - \psi_k^n) + C_{k,k+1}(\psi_{k+1}^n - \psi_k^n)}{\Delta t}. \end{aligned} \quad (16)$$

Discretizing the eddy flux parameterization from Equation 15, we obtain

$$F_k^\psi = -\tilde{\rho}_{k-1} K_k^z \frac{\psi_k^n - \psi_{k-1}^n}{\Delta \tilde{z}_{k-1}}. \quad (17)$$

This can be inserted into the left-hand side of Equation (16). Sorting both sides by terms of  $\psi_{k-1}^n, \psi_k^n, \psi_{k+1}^n$  and

comparing their prefactors gives

$$\begin{aligned} C_{k,k-1} &= \Delta t \frac{\tilde{\rho}_{k-1} K_k^z}{\rho_k \Delta z_k \Delta \tilde{z}_{k-1}}, \\ C_{k,k+1} &= \Delta t \frac{\tilde{\rho}_k K_{k+1}^z}{\rho_k \Delta z_k \Delta \tilde{z}_k}, \\ C_{k,k} &= 1 - C_{k,k-1} - C_{k,k+1}. \end{aligned} \quad (18)$$

Note, when simplified for constant (i.e., height-independent) density  $\rho$ , these terms inserted into the  $\psi$  tendency equation (Equation 16) match the local contribution of the corresponding equation in the ACM2 scheme (cf. Pleim, 2007a, his equation 10). So far, no assumptions on the local exchange coefficients  $K_k$  have been made, so that they can still be chosen arbitrarily to derive the corresponding local updraft, downdraft, and diagonal elements of the matrix  $C$  corresponding to the first, second, and third part of Equation 18. For the eddy coefficients, we choose the following parameterization after Pleim (2007b):

$$\begin{aligned} K_k^z &= K_0 + \left| \frac{\sqrt{(u_k - u_{k-1})^2 + (v_k - v_{k-1})^2}}{z_k - z_{k-1}} \right| \\ &\times \begin{cases} \left(1 - \frac{Ri_k}{Ri_c}\right)^2 l^2 & \text{if } Ri_k > 0 \\ \left(1 - \frac{Ri_k}{4}\right)^{\frac{1}{2}} l^2 & \text{if } Ri_k \leq 0 \end{cases} \quad \text{with } l = \frac{\kappa z_k \lambda}{\kappa z_k + \lambda} \end{aligned} \quad (19)$$

Here, the minimum eddy coefficient is chosen as  $K_0 = 0.05 \text{ m}^2 \cdot \text{s}^{-1}$ , and for the turbulent length scale  $l$  after Blackadar (1962) we set  $\lambda = 250 \text{ m}$ .  $Ri$  is the local gradient Richardson number

$$Ri_k = \frac{2g}{\theta_{v,k} + \theta_{v,k-1}} \frac{(\theta_{v,k} - \theta_{v,k-1})(z_k - z_{k-1})}{(u_k - u_{k-1})^2 + (v_k - v_{k-1})^2}. \quad (20)$$

As in the ACM2 scheme (cf. Pleim, 2007a; Pleim and Chang, 1992), we assume that, different from the updrafts, the downdrafts are less localized and much weaker so that they can be simulated by local turbulence. Hence, in the transilient matrix  $C$ , we apply only mixing terms directly below the diagonal. This simplifying assumption is justified by large-eddy simulations (LES) and observations as well. LES experiments by Ebert *et al.* (1989) suggest a pronounced asymmetry with strong nonlocal updrafts and weak local downdrafts, at least when not restricting to short time scales, when all motions become short ranging and, thus, local. Similar LES results are reported by Schumann (1989). Using a Doppler LIDAR, Ansmann *et al.* (2010) found that the observed updrafts have higher vertical velocities and smaller horizontal extents than the downdrafts. Lareau *et al.* (2018) concludes the same from

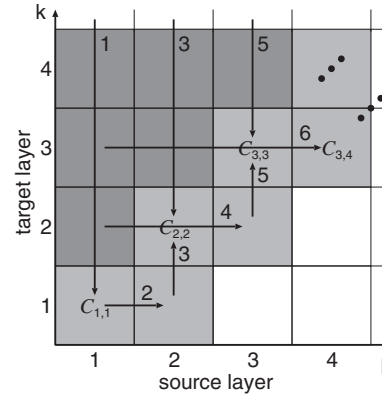


**FIGURE 3** Iterative method to determine diagonal and subdiagonal (subsidence) matrix elements (light gray) in accordance with mass and  $\psi$  conservation. Dark-gray elements are given by the updraft and local eddy mixing parameterization, and white elements are zero. The arrows denote along which row or column the conservation laws (Equation 11) are to be applied to determine the matrix element pointed to. Numbers denote the order of the single steps. For more details see text

the positive skewness of the vertical velocity distribution observed by LIDAR.

To fulfill the total mass and  $\psi$  conservation (cf. Equation 11), the missing diagonal and subsidence terms can be determined by using a recursive procedure (Figure 3). From the column sum criterion (Equation 11, left) of column 1,  $C_{1,1}$  is determined (arrow no. 1). Then,  $C_{1,2}$  follows from the row sum criterion (Equation 11, right) of row 1 (arrow no. 2).  $C_{2,2}$  is calculated from its corresponding column sum criterion for column 2 (arrows no. 3), then  $C_{2,3}$  follows from the row sum criterion of row 2 (arrow no. 4), and so on. For the last element  $C_{N_z, N_z}$ , which is determined from the column sum criterion of column  $N_z$ , the corresponding row sum criterion (row  $N_z$ ) is automatically fulfilled by construction, although the equation system appears to be overdetermined ( $2N_z$  row and column criteria for  $N_z + (N_z - 1) = 2N_z - 1$  diagonal and secondary diagonal matrix elements). Because the derivation of Equation 18 includes the conservation laws of total mass and  $\psi$ , i.e., the row and column sum criteria (Equation 11), choosing a value for  $C_{k,k-1}$  and following the construction procedure above leads to the same values for  $C_{k,k}$  and  $C_{k,k+1}$  as Equation 18. To ensure that the transilient matrix simulates physical mixing, the matrix elements must satisfy  $0 \leq C_{k,l} \leq 1$  (cf., e.g., Stull, 1993). Because  $C_{k,l}$  depends on the time step  $\Delta t$ , this can be translated into a time step limitation. Thus, the following automatic time step reduction method is applied:

Reduce the original time step  $\Delta t$  by an integer factor  $n$ , such that the upper-triangle elements of  $C$  (upward transports), which are all proportional to  $\Delta t$ , result in diagonal

elements between 0.5 and 1. This guarantees physical reasonable mixing (i.e.,  $C_{ij} < 1$ ). From Equation 11 it follows that the reduction factor  $n$  results in

$$n = \max(1, \text{integer}(0.5 + 2c_{\max})) \quad \text{with} \quad c_{\max} = \max_k \left( \sum_l |C_{l,k} m_l / m_k|, \sum_l |C_{k,l}| \right) \quad (21)$$

After this scaling, we reconstruct the diagonal and downdraft elements as already described above, that is, with Equation (11), after the method shown in Figure 3. We then replace the original matrix  $C$  and time step  $\Delta t$  by

$$C' = C^n \quad \text{and} \quad \Delta t' = \frac{\Delta t}{n}. \quad (22)$$

### 2.2.2 | Three-dimensional turbulence

So far, the transilient matrix is applied to the vertical direction. To enable the scheme to represent horizontal turbulence as well, the matrix formalism has to be applied to the horizontal directions  $x$  and  $y$ . In principle, a trivial solution would be to extend the one-dimensional Equation (5) to three dimensions. However, this would require the solution of an equation involving a six-dimensional matrix  $C_{k,l;m,n;p,q}$  with one index pair for each dimension, but most of the horizontal nonlocal mixing elements being zero anyway. Because this would be too expensive in terms of computation time and memory, we choose an operator splitting approach with one one-dimensional matrix equation for each dimension.

Since each grid column  $(i, j)$  has its individual vertical mixing matrix  $C^z$ , henceforth we add these indices as a superscript. These are not to be confused with the row/column indices  $k, l$ . Analogously to the vertical mixing matrix being defined at each grid column  $(i, j)$  on a horizontal plane, the horizontal  $x$  mixing matrix  $C^x$  is defined at each grid row  $(j, k)$  in a meridional  $y$ - $z$  cross section with matrix elements  $(i, l)$  and the  $y$  mixing matrix  $C^y$  is defined at each grid row  $(i, k)$  in a zonal  $x$ - $z$  cross section with matrix elements  $(j, l)$ :

$$\psi_{i,j,k}^* = \sum_{l=1}^{N_z} C_{k,l}^{z,i,j} \psi_{i,j,l}^n \rightarrow \frac{\partial \psi}{\partial t} \Big|_{\text{turb},z} = \frac{1}{\Delta t} (\psi_{i,j,k}^* - \psi_{i,j,k}^n) \quad (23)$$

$$\psi_{i,j,k}^{**} = \sum_{l=1}^{N_y} C_{j,l}^{y,i,k} \psi_{i,l,k}^n \rightarrow \frac{\partial \psi}{\partial t} \Big|_{\text{turb},y} = \frac{1}{\Delta t} (\psi_{i,j,k}^{**} - \psi_{i,j,k}^n) \quad (24)$$

$$\psi_{i,j,k}^{***} = \sum_{l=1}^{N_x} C_{i,l}^{x,j,k} \psi_{l,j,k}^n \rightarrow \frac{\partial \psi}{\partial t} \Big|_{\text{turb},x} = \frac{1}{\Delta t} (\psi_{i,j,k}^{***} - \psi_{i,j,k}^n) \quad (25)$$

$$\frac{\partial \psi}{\partial t} \Big|_{\text{turb}} = \frac{\partial \psi}{\partial t} \Big|_{\text{turb},x} + \frac{\partial \psi}{\partial t} \Big|_{\text{turb},y} + \frac{\partial \psi}{\partial t} \Big|_{\text{turb},z} \quad (26)$$

With  $N_x, N_y, N_z$  denoting the numbers of grid boxes in each direction of the model domain (and assuming  $N_x = N_y \gg N_z$  for simplicity), this reduces the total number of matrix elements from  $N_x^2 N_y^2 N_z^2 = N_x^4 N_z^2$  to  $N_x N_y \cdot N_z^2 + N_y N_z \cdot N_x^2 + N_x N_z \cdot N_y^2 \approx 2N_x^3 N_z$ . Since the tendencies for each dimension are all derived from the same state  $\psi_{i,j,k}$  and are summed up for the total turbulent tendency, the operator splitting is independent of the ordering of the single contributions. Quantitatively, the horizontal turbulent forcing could be determined from the three-dimensional TKE equation, as, for example, in Zhang *et al.* (2018), who derive horizontal eddy coefficients from a formula blending Smagorinsky diffusion and diffusivity based on TKE.

We follow a more geometrically motivated approach by initiating horizontal mixing only in regimes where enough vertical turbulent motions start or arrive. This reflects the conceptional model of turbulent motions as closed circulating whirls and prevents the scheme from starting turbulence too often and in too many grid boxes. A possible drawback of this approach may be that purely horizontal eddies cannot be represented. We first average the corresponding elements of  $C^z$  in each layer  $k$  for eddies interacting with either  $k_{\text{PBL}} - 1$  layers (nonlocal turbulence) for layer  $k$  within the PBL or two layers (local turbulence) for layer  $k$  in the free atmosphere. Considering a factor of 2 for two fluxes (each departing and arriving) per layer and the number of dimensions, this provides us with a measure  $\mathcal{H}$  of the horizontal turbulent activity of each grid box  $(i, j, k)$ :

$$\mathcal{H}_{i,j,k} = \frac{1}{6} \frac{1}{k_{\text{PBL}} - 1} \left( \sum_{\substack{l=1 \\ l \neq k}}^{k_{\text{PBL}}-1} C_{l,k}^{z,i,j} + \sum_{\substack{l=1 \\ l \neq k}}^{k_{\text{PBL}}-1} C_{k,l}^{z,i,j} \right) \quad \text{for } k < k_{\text{PBL}} \quad (27)$$

$$\mathcal{H}_{i,j,k} = \frac{1}{12} \left( \sum_{l=k \pm 1} C_{l,k}^{z,i,j} + \sum_{l=k \pm 1} C_{k,l}^{z,i,j} \right) \quad \text{for } k \geq k_{\text{PBL}}. \quad (28)$$

This auxiliary quantity  $\mathcal{H}_{i,j,k}$  is then averaged over the nearest neighbors in  $x$  or  $y$  direction (cf. Figure 4). To avoid double counting, for a specific grid location  $i$  only eddies from the (direct) neighbors have to be considered, that is, only  $\mathcal{H}_{i-1,j,k}$  and  $\mathcal{H}_{i+1,j,k}$ . So, each  $\mathcal{H}_{i,j,k}$  is used only twice, consistent with the fact that the number of adjacent grid boxes in  $x$  direction that a large local eddy may at maximum interact with is only two (rather than three) when iterating along  $i$ .

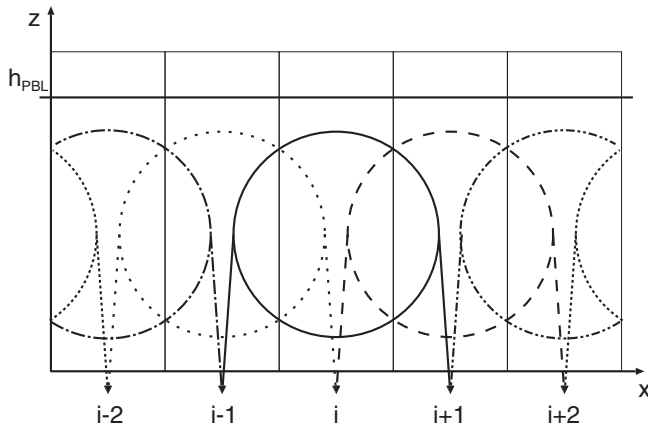


**FIGURE 4** Sketch of the problem of how to avoid double counting when averaging the horizontal turbulence activities  $H$ . In each layer, for a grid column at index  $i$  only the eddies of the neighbors  $i \pm 1$  are considered. This in turn guarantees that each  $H_{i,j,k}$  is only used twice, as it is nonlocal to only two grid columns (rather than three). For the  $y$  direction (index  $j$ ) an analogous reasoning holds

The parameterization of horizontal turbulence should also take the horizontal grid size  $\Delta x, \Delta y$  into account. Honnert *et al.* (2011) analyzed LES results to estimate the partitioning of the dynamics and thermodynamics into grid-scale and subgrid-scale fluxes as they would appear in mesoscale models with different horizontal grid sizes. From their fit formulas, we derived scaling factors  $f(\delta_x), f(\delta_y)$  with  $\delta_x = \Delta x/h_{PBL}$ ,  $\delta_y = \Delta y/h_{PBL}$  accordingly.

$$C_{i,l}^{x,j,k} = \frac{1}{2}(\mathcal{H}_{i-1,j,k} + \mathcal{H}_{i+1,j,k}) \frac{\delta_x^2 + 0.02 \cdot \delta_x^{1/4}}{\delta_x^2 + 0.02 \cdot \delta_x^{1/4} + 0.025} \quad (29)$$

$$C_{j,l}^{y,i,k} = \frac{1}{2}(\mathcal{H}_{i,j-1,k} + \mathcal{H}_{i,j+1,k}) \frac{\delta_y^2 + 0.02 \cdot \delta_y^{1/4}}{\delta_y^2 + 0.02 \cdot \delta_y^{1/4} + 0.025} \quad (30)$$

### 3 | OBSERVATIONS

To check the model results over homogeneous terrain, we use observational data from the Cooperative Atmosphere Surface Exchange Study (CASES-99) campaign (Poulos *et al.*, 2002). This campaign was performed in the Walnut River watershed covering an area of about 100 km meridionally and 60 km zonally east of Wichita, Kansas, USA during October 1–31, 1999. A corresponding map with the locations of observational stations and larger cities is shown in Figure 5. Data are publicly available from the NCAR/UCAR Earth Observing Laboratory website ([https://www.eol.ucar.edu/field\\_projects/cases-99](https://www.eol.ucar.edu/field_projects/cases-99)) and the Argonne National Laboratory (ANL) and its Atmospheric Boundary Layer Experiments (ABLE) Facility (<https://www.atmos.anl.gov/ABLE/casesarchive.html>). Among the CASES-99 datasets, we use

- Radiosonde data at Leon, Smileyberg, Beaumont, and Eldorado: temperature, pressure, moisture, and horizontal wind profiles at high vertical resolution.

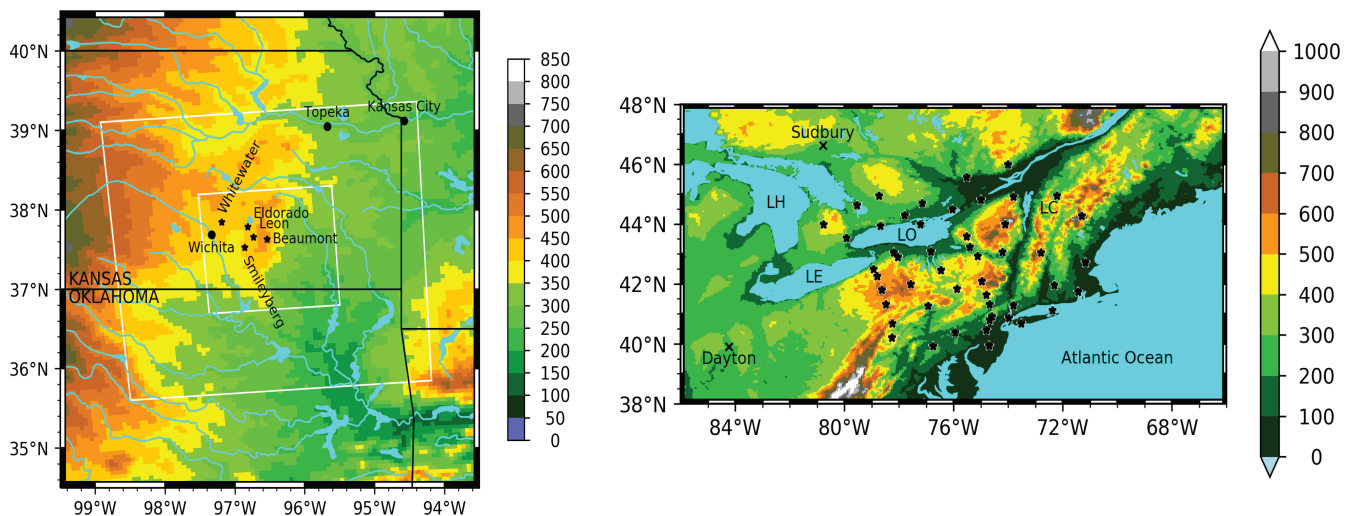


**FIGURE 5** Maps of the observation areas of the CASES-99 campaign (left) and the CAPTEX campaign (right) with locations of observational stations (asterisks). The left map also shows the locations of some larger cities (filled circles) and the boundaries of the two innermost simulation nests (white boxes). In the right map, the locations of tracer release, Dayton and Sudbury, are displayed as crosses. Also labeled are Lake Huron (LH), Lake Erie (LE), Lake Ontario (LO), and Lake Champlain (LC)

LeMone *et al.* (2002) state an accuracy of 0.5 K for temperature and 5% for relative humidity or up to  $0.8 \text{ g kg}^{-1}$  for specific humidity (including turbulence-induced deviations from the local average) for the precursor campaign CASES-97. Unfortunately, there is no estimate of the accuracy of horizontal wind.

- Energy balance/Bowen ratio (EBBR) station at Whitewater: surface fluxes of sensible and latent heat with an accuracy of 10%.
- Soil temperatures (0–5 cm deep) with an accuracy of 0.5 K and volumetric soil moistures (at 2.5 cm depth), at the EBBR station in Whitewater and at Smileyberg, each averaged over an array of five sensors.

For simulations over more complex terrain, we use real cases from the Cross Appalachian Tracer Experiment (CAPTEX) (Ferber *et al.*, 1986), in which a passive tracer (perfluoromonomethylcyclohexane) was released from locations north and west of the Appalachians, Sudbury in Canada ( $46.62^\circ\text{N}$ ,  $80.78^\circ\text{W}$ ) and Dayton in the USA ( $39.90^\circ\text{N}$ ,  $84.22^\circ\text{W}$ ). The tracer was observed at 84 stations scattered on both sides of the mountain range. We use five cases of tracer releases in September and October 1983 during different weather situations when the observation stations were located downstream of either Dayton or Sudbury (Table 1).

In all cases, the tracer was emitted into a well-mixed convective PBL, that is, in the early afternoon from Dayton and after a cold front passage (although at night) from Sudbury. After each tracer release, the observation stations were successively activated and the next release was not started before the tracer had left the observation area (see Ferber *et al.* (1986) for more details). CAPTEX tracer emission and measurement data are publicly available from <https://www.arl.noaa.gov/research/dispersion/datem>. Synoptic information is obtained from NOAA Weather Prediction Center (WPC) surface analysis maps available at [https://www.wpc.ncep.noaa.gov/archives/web\\_pages/sfc/sfc\\_archive.php](https://www.wpc.ncep.noaa.gov/archives/web_pages/sfc/sfc_archive.php).

## 4 | RESULTS

Several real case simulations have been carried out with the WRF model including the NLT<sub>3D</sub> scheme as well as the ACM2 and MYNN scheme as turbulence parameterizations. These simulations have been compared with observations from the CASES-99 and CAPTEX campaigns.

### 4.1 | Homogeneous terrain

To check the general validity of the scheme, we start with the classical experiment of simulating the PBL and its diurnal cycle over homogeneously vegetated and relatively flat terrain in radiation-dominated weather conditions (i.e., without clouds). We have chosen three real cases each of 36 hr duration from the CASES-99 campaign (over prairie grass land). For all cases, the WRF model is initialized in the early morning (local time) to enable the full evolution of the convective PBL. The three cases comprise time periods of 36 hr each, starting at 1200 UTC (0600 LT) on October 9, 11, and 23, 1999.

As Figure 5 shows, the orography is relatively flat, although with a weak slope to the west. The river basins are usually very shallow. For the sake of simplicity, we have chosen clear-sky periods for our simulations. For the nested WRF simulations, we use a horizontal grid size ratio of 1:5:3:3 starting from the driving ERA5 analyses with a  $0.25^\circ$  grid, that is,  $0.05^\circ$ ,  $0.0167^\circ$ , and  $0.00556^\circ$  ( $\approx 5 \text{ km}$ ,  $1.7 \text{ km}$ , and  $600 \text{ m}$ ) for the three nested WRF domains, respectively. Starting with the outermost domain, the three nests are 130, 211, and 271 grid boxes wide in both zonal and meridional direction and are all centered at  $37.5^\circ\text{N}$  and  $96.5^\circ\text{W}$ . The time step of  $\Delta t = 30 \text{ s}$  in the outermost domain is reduced for the nests by the same ratio as the horizontal grid, that is,  $10 \text{ s}$  for the intermediate and  $10/3 \text{ s}$  for the innermost domain. To facilitate the interpretation of the results, there is no feedback from inner finely resolved domains to outer coarsely resolved domains.

**TABLE 1** Tracer releases during the CAPTEX campaign (1983) used in this study and corresponding WRF simulation periods

Release	Release period (UTC)	Simulation period (UTC)	Location of release	Amount (kg)	Winds
1	September 25, 1705–2005	September 25, 1200–September 28, 0000	Dayton	201	SW, later W ... NW
2	October 02, 1900–2200	October 02, 1200–October 04, 1800	Dayton	201	SW, later W
3	October 14, 1600–1900	October 14, 1200–October 16, 1800	Dayton	199	SW, soon W ... NW
4	October 26, 0345–0645	October 25, 1200–October 27, 2100	Sudbury	180	NW, later W
5	October 29, 0600–0900	October 28, 1200–October 30, 2100	Sudbury	183	NW, later N

Note: Local time is UTC – 6 hr.



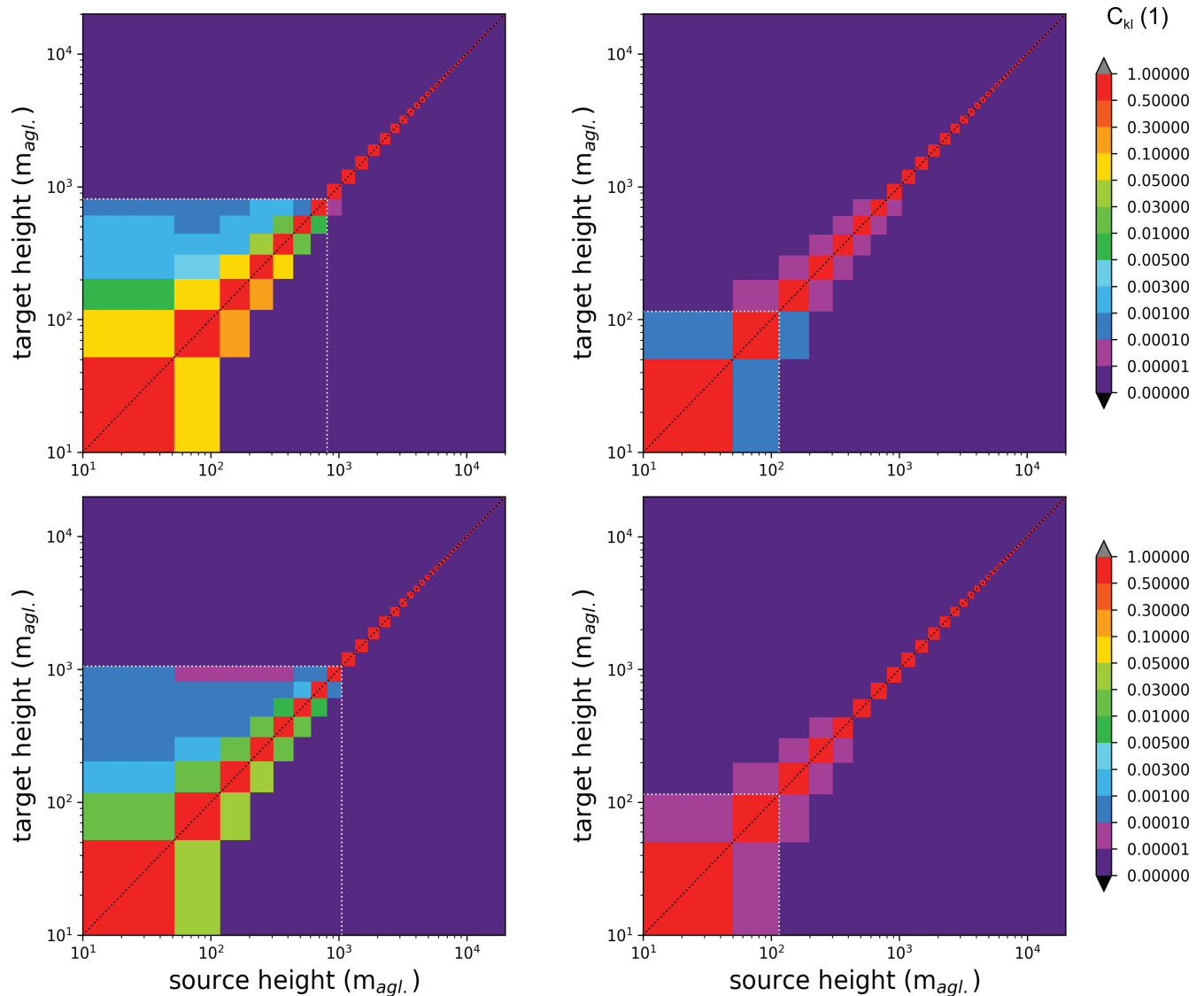


**FIGURE 6** Two transilient matrices typical for the daytime convective PBL (1500 LT, left column) and the stable nighttime PBL (0400 LT, right column; both on October 12, 1999) for  $\Delta x=1.7$  km (top row) and  $\Delta x=600$  m (bottom row), all at the same location. The matrix elements are already multiplied with  $\Delta t = 10$  s (top row) and 3.3 s (bottom row) to show the direct exchange fractions between the source and target heights. The dotted white lines denote the PBL top height, and the dotted black line marks the diagonal

#### 4.1.1 | Transilient matrix

To check the proper behavior of the structure of the transilient matrix elements, we here analyze two typical vertical mixing matrices (Figure 6). The matrix from the afternoon shows a convective PBL of about 800 m depth with strong nonlocal updrafts and local down-drafts. Whereas the downdraft is local by construction (to reflect slow and spatially widespread downward transport), the updraft is nonlocal by the unstable/convective stratification via the parameterization with the nonlocal Richardson number.

Typical structures of the transilient matrix claimed by idealized high-resolved LES studies (Ebert *et al.*, 1989,

also cf. their figures 17a and 5d/e) are (a) asymmetry referring to the diagonal, (b) maxima below the diagonal (downward transport) within the PBL, and (c) maxima at the ends of the cross-diagonal through the depth of the PBL (i.e., square left and below the white dotted lines in Figure 6).

Whereas property (a) is clearly fulfilled by the mixing matrix, properties (b) and (c) are only slightly indicated by the matrix. Concerning (b), downdrafts are generally stronger than the single updrafts. Property (c) is at least fulfilled for the updrafts (top left corner in the white square denoting the PBL in Figure 6) and as the strongest downdrafts are located near the surface. Since there is no explicit entrainment parameterization included in  $NLT_{3D}$ ,

**TABLE 2** Order of magnitude of matrix elements during convective PBL situations sorted by different grid sizes and local/nonlocal transports (on October 11, 1999, 1500 LT)

	$\Delta x = 5 \text{ km}$	$\Delta x = 1.7 \text{ km}$	$\Delta x = 600 \text{ m}$
Local mixing	0.01–0.3	0.007–0.2	0.0005–0.05
Nonlocal updrafts	0.003–0.03	0.001–0.01	0–0.003

an important property of the scheme is that the turbulent reduction of the PBL top inversion by upward mixing of heat from the surface is controlled and facilitated by vertically nonlocal mixing.

The typical values of the matrix elements during daytime in convective PBL situations are presented in Table 2. One significant feature is that local mixing by small-scale eddies is still about a factor 3–20 larger than nonlocal updrafts. However, local eddy mixing requires a longer time to reach the PBL top from the ground (about 10 levels distance) with dilution of the initial surface air at every mixing stage. Thus, for vertically long-distance transports, local and nonlocal mixing are still of comparable effectivity. Starting from  $\Delta x = 5 \text{ km}$  over  $1.7 \text{ km}$  down to  $600 \text{ m}$ , matrix elements for both local mixing and nonlocal updrafts decrease with the grid size, reflecting the lesser need for parameterized mixing at smaller grid sizes.

At nighttime, only a weak local eddy activity at least two orders of magnitude weaker than the exchange coefficient at daytime is present in the shallow and stable PBL. Above the PBL, matrix elements on the secondary diagonal due to local eddy activity are usually in the order of about  $10^{-6}$ .

#### 4.1.2 | Surface fluxes

Figure 7 compares the temporal evolution of the surface heat fluxes as simulated by WRF including the three PBL schemes with the observations during the three real case time periods. To obtain representative simulation values, simulation results of each domain have been averaged over the grid point containing the station location and its neighbors covering a square of about  $32 \text{ km}$  width (in the following for the medium grid size domain, that is, with  $\Delta x = 1.7 \text{ km}$ ).

During these days, the CASES study area is always located in an area of weak pressure gradients. On October 9, 1999, the domain is in the warm air sector of a low over southern Canada. The prevailing high-pressure influence is practically not disturbed by two weak cold fronts passing the domain in the morning of October 10 and afternoon of October 12, 1999. No significant clouds or even

precipitation has been formed. Winds within the PBL are of the order of only a few  $\text{m}\cdot\text{s}^{-1}$ .

As the diurnal cycle of the surface fluxes in Figure 7 (top) confirms, the weather situation in all three cases was clearly radiation dominated with no or only a few small and thin clouds in the sky. During all cases, simulated surface fluxes of sensible heat are underestimated by about  $30 \text{ W}\cdot\text{m}^{-2}$  at the maximum around local noon. This qualitatively agrees with Svensson *et al.* (2011), who compared 30 simulations from different NWP models and PBL schemes (although ACM2 and MYNN unfortunately were not among them) with observations during a part of the CASES-99 period (59 hrs starting at 1600 LT, October 22, 1999). They found that their participating models underestimated the observed daytime flux of sensible heat (by up to about  $100 \text{ W}\cdot\text{m}^{-2}$ ) and overestimated the nighttime flux of sensible heat (by up to about  $50 \text{ W}\cdot\text{m}^{-2}$ ) for the above-mentioned part of the CASES-99 period. In our case, the deviations are often only slightly beyond the accuracy of the observations. Generally, the simulated surface fluxes underestimate the observations by less than  $30 \text{ W}\cdot\text{m}^{-2}$ . During nighttime, simulated surface fluxes mostly well reproduce the observations.

However, it should be noted that such comparisons are difficult since the results depend on many details of the simulations. We perform simulations coupled to the Noah land-surface model, whereas Svensson *et al.* (2011) prescribe the surface temperature. Shin and Hong (2011) also perform simulations of the CASES-99 campaign coupled to the Noah land-surface model, but use an older WRF version (v3.2) and a different radiation scheme (RRTMG) and driving boundary data in their extensive comparison study including a number of different PBL schemes. Their simulations more or less *overestimate* surface sensible and latent heat fluxes by up to  $100 \text{ W}\cdot\text{m}^{-2}$ . Steeneveld *et al.* (2008) employ the MM5 model, which was the predecessor of WRF, and find a significant dependence of the bias of the surface sensible heat flux from the details of the vegetation parameterization.

The differences between the three PBL schemes (NLT<sub>3D</sub>, ACM2, and MYNN) are generally small ( $<10 \text{ W}\cdot\text{m}^{-2}$ ). The same holds for the simulations with the three different grid box sizes (nested domains). On October 12, 1999 in particular, the innermost nest ( $\Delta x = 600 \text{ m}$ ) tends to form some clouds and fine structure in the heat flux curves and the sensible heat fluxes among the three PBL schemes differ by up to  $25 \text{ W}\cdot\text{m}^{-2}$  during the last hours before sunrise (not shown). This may be related to the passage of the weak cold fronts mentioned above.

So, in summary, for all cases and all three PBL schemes, surface heat fluxes tend to be slightly too low; that is,

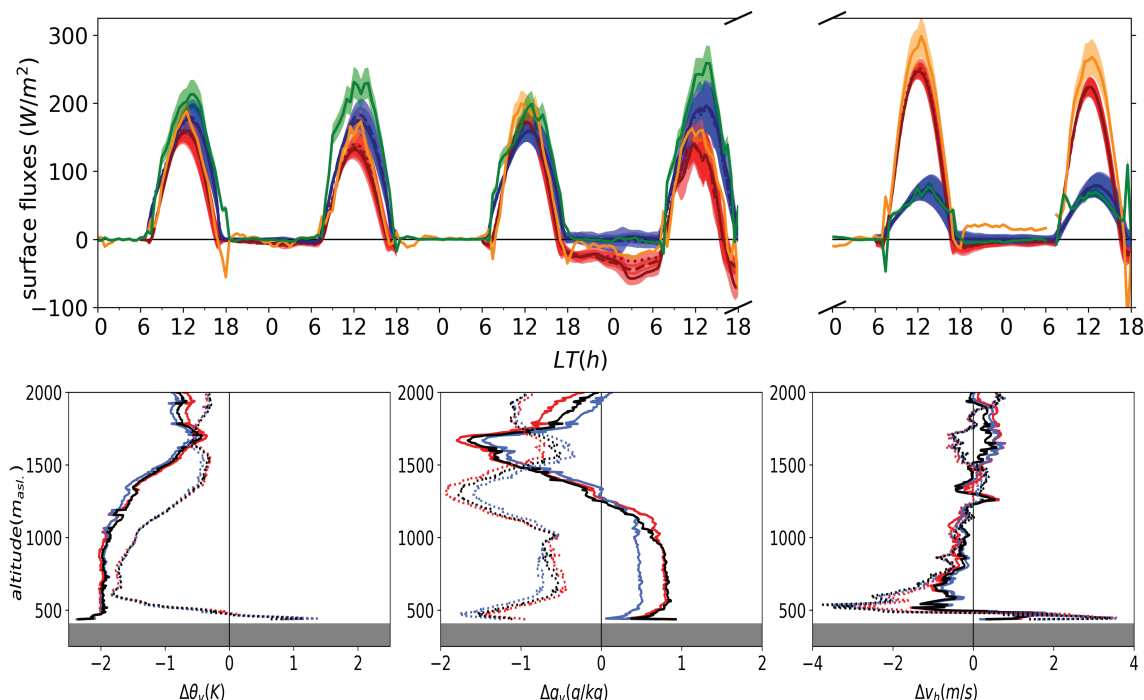


**FIGURE 7** Comparison of surface fluxes and profiles between observations and WRF medium-resolution simulations (averaged over  $32\text{ km} \times 32\text{ km}$  areas centered at each station and all analyzed cases of CASES-99). Top row: temporal evolution of surface fluxes of sensible heat (WRF: red, EBBR: orange) and latent heat (WRF: blue, EBBR: green) at the EBBR station at Whitewater. Simulations with NLT<sub>3D</sub> (solid), ACM2 (dashed), and MYNN scheme (dotted). The shaded bands represent the standard deviation of the simulation values over the averaging area/accuracies of the observations. Bottom row: averaged differences between profiles of virtual potential temperature, specific humidity, and horizontal wind simulated by WRF with the NLT<sub>3D</sub> (red), ACM2 (light blue), and MYNN (dark green) schemes and measured by radiosondes. Difference profiles WRF–radiosondes during daytime are solid, and those during nighttime are dotted

the heat and moisture exchange between the soil and the lowermost atmosphere is slightly too weak.

#### 4.1.3 | Profiles from radiosondes and relations to surface/soil quantities

During the simulation period of  $3 \times 36\text{ hr}$ , a total of 63 radiosonde ascents with high vertical resolution took place from Smileyberg, Eldorado, Leon, and Beaumont. Unfortunately, there were no radiosonde ascents from Whitewater, where the flux measurements were conducted. However, soil temperatures and moisture were observed at Whitewater and Smileyberg, both with the same type of instruments. To better compare the surface and soil observations at Whitewater and the radiosonde sites, simulation results of soil temperatures and moisture have been averaged over a  $32\text{ km}$ -wide square centered at Whitewater and over a rectangular domain containing the  $32\text{ km}$ -wide neighborhood of the four radiosonde sites. The uppermost soil layer of fixed  $10\text{ cm}$  depth (NOAH scheme) from which the simulation results are extracted is judged to be roughly comparable to the depths of the observed soil

temperatures (integrated over  $0\text{--}5\text{ cm}$ ) and soil moisture ( $2.5\text{ cm}$ ).

The measured profiles of temperature, pressure, relative humidity, and horizontal wind components  $u, v$  are converted to virtual potential temperature  $\theta_v$ , specific humidity  $q_v$ , and horizontal wind  $v_h = \sqrt{u^2 + v^2}$ . These profiles are classified into 18 daytime profiles (0900–1700 LT) and 42 nighttime profiles (1900–0700 LT). Simulations are averaged each over the grid box containing the location of the radiosonde launch and the neighboring grid boxes covering about  $15\text{ km}$  in each direction resulting in a  $32\text{ km}$ -wide averaging domain. This is to roughly consider the horizontal displacement of the radiosonde during a typical ascent time of  $1,100\text{--}1,500\text{ s}$  with typical horizontal winds of less than about  $10\text{ m s}^{-1}$ . Figure 7 shows the resulting mean differences between the simulation results and the corresponding observations (again from the medium grid size domain). The results from the two other simulations (finer and coarser grid) look very much the same. Although the absolute differences are relatively small ( $<2\text{ K}$  for  $\theta_v$  and  $<2\text{ g kg}^{-1}$ ) and/or limited to a thin vertical layer (as for  $v_h$ ), it is interesting to

analyze them within the scope of the surface fluxes and soil temperatures and moistures passed from the soil and surface parameterization to the PBL schemes.

Figure 7 illustrates that modeled sensible and latent fluxes underestimate the observations, especially during daytime. We now assume that this low bias is of larger spatial scale or is even more generally found (at least for the time and area of the CASES-99 campaign), as Svensson *et al.* (2011) suggest.

For October 9–12, 1999, at daytime, observed soil temperatures at Whitewater with maximum values of 21–22°C are up to 3 K warmer than at Smileyberg, while at nighttime, values at both locations are very similar (minimum temperatures of 15–17°C). With very little difference among the three PBL schemes and for both locations, simulated soil temperatures with maximum values of 23–25°C in the afternoon and 13–15°C in the early morning show a warm bias of up to 3 K at daytime and 1–3 K at nighttime (not shown).

At daytime, the warm bias of the soil temperature and the cold bias of the near-surface air at the radiosonde sites in the simulations mean a too high temperature difference in the simulations compared with the observations. This is consistent with the low bias of the simulated sensible heat flux (cf. Figure 7). However, for moisture, the signs of the simulation biases do not allow for such a distinct statement. Because the moisture of both the soil and near-surface air are predominantly simulated too high (by about  $0.02\text{--}0.05\text{ m}^3\cdot\text{m}^{-3}$ , not shown), there is no qualitative assessment in terms of a too high or too low latent heat flux possible. The high bias in the near-surface winds generally suggests that the simulated friction velocity is underestimated. As single modeled profiles and radiosonde profiles (not shown) reveal, within the PBL the observed horizontal wind profile is more structured and often exhibits stronger winds in the mid and lower PBL and weaker winds just above the ground when compared with the simulations. This results in the two peaks in the difference plot and means a too strong momentum mixing in the PBL and a too weak momentum flux at the surface.

In summary, as this is the case for all three PBL schemes, the soil scheme as the driver for soil temperatures and moistures and the surface scheme driving the surface fluxes for given differences between soil and air properties become candidates for that deviation.

At nighttime, biases of the near-surface air and soil temperatures are opposite to the daytime situation, but significantly smaller, consistent with the smaller deviation in the sensible heat flux. In the higher PBL decoupled from the surface (residual layer), the cold bias from the previous day is preserved. A conclusion for the latent heat flux is again difficult, this time because there is no uniform sign in the bias at the radiosonde sites and Whitewater.

#### 4.1.4 | Differences between PBL schemes

Generally, the three PBL schemes show relatively similar behavior in quantities that are horizontally homogeneous. One of the most sensitive quantities in a PBL scheme is the PBL depth. In particular, when the convective PBL decays around and after sunset, inhomogeneities due to spatial surface variations are expected. Figure 8 shows the PBL depths as determined by each individual scheme at 1800 LT. At most places on the map, the convective PBL has at least started to decay or is already shallow and stable, except for some city areas (e.g., Kansas City, Topeka, Wichita) and the southeastern part of the domain, which is, different from the rest, partially covered by forests. The heat islands or reservoirs still maintain the convective PBL with depths of about 500–1,000 m for several hours into the night.

So, apart from large-scale averages, locally significant differences between the three schemes show up. Whereas the PBL depths simulated by the NLT<sub>3D</sub> and ACM2 scheme look qualitatively similar, the PBL as represented by the MYNN scheme is much more convective at that time and also decays much slower. Even comparing NLT<sub>3D</sub> and ACM2 now shows somewhat higher PBL depths and, thus, more convective activity in the ACM2 results compared with NLT<sub>3D</sub>. These findings clearly motivate a comparison of the three schemes over inhomogeneous terrain.

#### 4.2 | Complex terrain

To analyze benefits of the NLT<sub>3D</sub> scheme, we now move to more complex terrain with inhomogeneous surface as, for example, found in the Appalachian mountain region, where the CAPTEX campaign took place. Since it cannot be expected that a model can ever reproduce specific local three-dimensional structures as found in point measurements (e.g., radiosondes) in such a domain, we seek a more integral measure with fewer dimensions. Such a quantity is a passive tracer as released in the CAPTEX campaign, transported along/across the Appalachians and then observed by ground stations (Figure 5).

The observed tracer concentrations will then be compared with the model results by means of geographical maps showing absolute values (direct temporal and spatially two-dimensional comparison) and time series of fraction skill scores (FSS) applying different threshold values (temporal and spatially one-dimensional comparison). In each case, the WRF simulations have been initialized with ERA5 reanalyses at the local morning (1200 UTC, i.e., 0600 LT) before the tracer emission to enable the model to build up a proper PBL and leave sufficient time for the decay of possible spin-up effects. This time, WRF is run



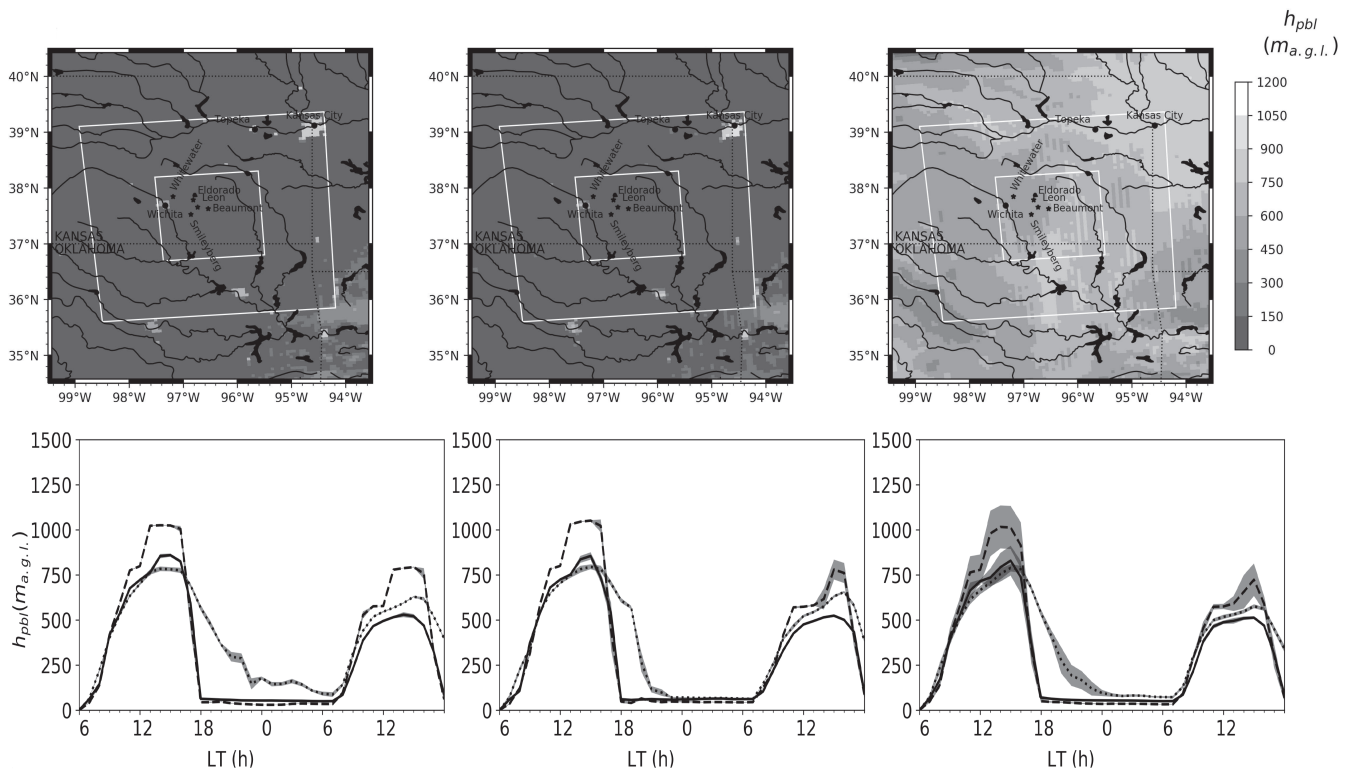


**FIGURE 8** Top row: maps of PBL depths at October 23, 1999, 1800 LT for the whole WRF domain (inner domains are marked by white frames) simulated with the NLT<sub>3D</sub> (left), ACM2 (center), and MYNN (right) scheme. Bottom row: Diurnal cycles of the PBL depths starting at October 23, 1999, 0600 LT simulated with the NLT<sub>3D</sub> (solid), ACM2 (dashed), and MYNN (dotted) scheme in the coarse (left), medium (center), and fine resolved domain (right). The shaded bands represent the standard deviation of the simulation values

with a single domain of 501 grid boxes zonally and 211 grid boxes meridionally (centered at 42.5°N, 77.5°W), a horizontal grid size of 5 km corresponding to 0.05° (1/5 of the ERA5 grid size), and a physical time step of 30 s. This is a compromise for grid sizes at least of the order of a few kilometers, and computational cost which will dramatically rise for finer resolution (including necessary nesting) of such a large domain covering the area across which the tracer moves.

#### 4.2.1 | Analysis of tracer transport

In cases 1, 2, and 3, the observation area is always located at the rear side of high-pressure systems located over the east coastal states of the United States. So, southwesterly winds prevail and the tracer has been released from Dayton, OH, thus that the observation network is located downstream. As an example, Figure 9 shows the temporal evolution of the tracer in case 3. As inspection of the observational data reveals, all partial tracer tendencies from the CAPTEX dataset are integer multiples of 0.0156 ng·m<sup>-3</sup>. So, we here take this value as a detection/resolution limit of the observations. Since also high values of (at least initially)

>100 ng·m<sup>-3</sup> are attained, we choose a logarithmic color scale.

During the first hours after release in Dayton (October 14, 1983, 1600–1900 UTC), the tracer is advected to the northeast about 1° south of Lake Erie. Initially, all three simulation results look similar, but then, after passing about 80°W, where the Appalachian mountain ridge becomes lower (<1,000 m asl.), a part of the tracer air mass in the simulation with the NLT<sub>3D</sub> scheme extends to the south and starts crossing the Appalachians (Figure 9 left). This agrees well with the observations. The ACM2 results at the same time only show a weak tendency of the tracer air mass to cross the mountains, and in the simulation with the MYNN scheme, the tracer has by far not reached 80°W yet at that time (October 15, 1983, 0100 UTC), which is in contradiction to the observation. These differences of the horizontal transport velocities of the tracer near the surface are closely connected with the different vertical mixing in the convective PBL:

A vertical cross section (Figure 10) along the direction of the horizontal transport (marked in Figure 9 by a black line) reveals that the PBL top height is highest in the simulation with the NLT<sub>3D</sub>, followed by the results from ACM2. With the MYNN scheme, the PBL is very shallow at the



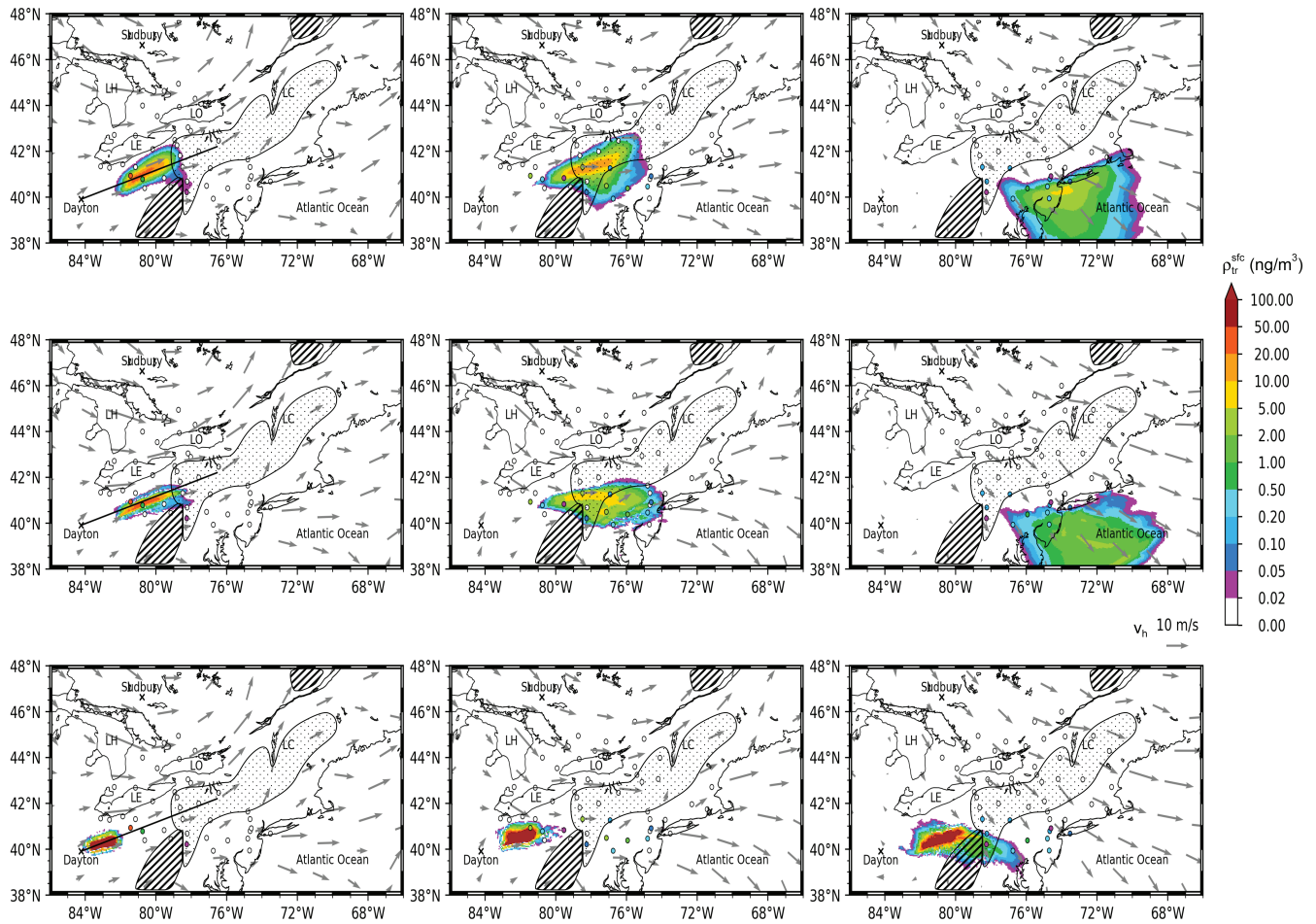


**FIGURE 9** Maps showing the temporal evolution of the tracer-containing air mass during case 3: Tracer partial densities in the lowermost model layer on October 15, 1983, 0100 (left column), 0600 (center column), and 1600 UTC (right column) simulated with WRF and the NLT<sub>3D</sub> (top row), ACM2 (center row), and MYNN scheme (bottom row) are color coded, colored circles denote observed values at station locations, and empty (white) circles show active stations observing less tracer than the detection limit (see text). Inactive stations (i.e., not measuring at the specified time) are not drawn in the map. The approximate boundaries of regions with relevant orography higher than 500 m a.s.l. are dotted, and higher than 700 m a.s.l. are hatched. Gray arrows denote the horizontal wind in the lowermost model layer (about 50 m deep) with only every 30th wind vector drawn.

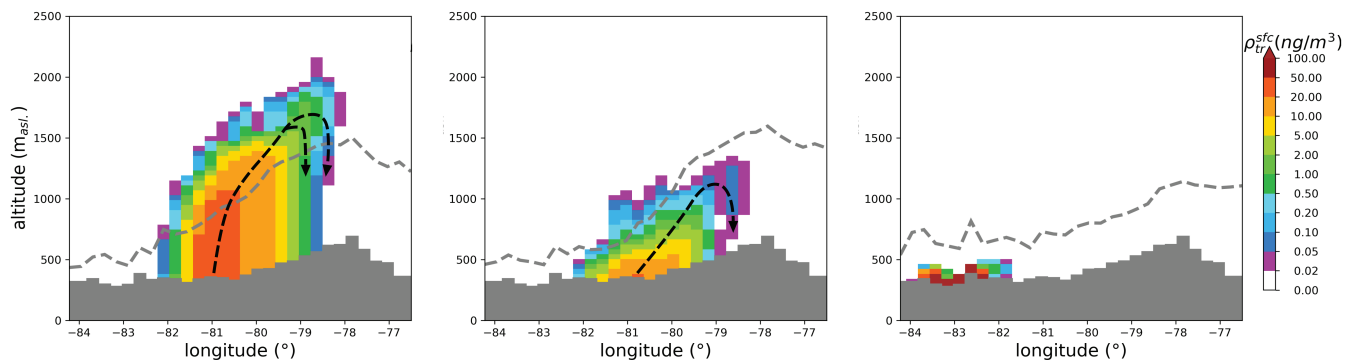


**FIGURE 10** Vertical cross section along the black line in Figure 9 (left) on October 15, 1983, 0100 UTC. The tracer partial densities as simulated with WRF and the NLT<sub>3D</sub> (left), ACM2 (center), and MYNN scheme (right) are color coded, and the underlying orography is shaded in gray. The dashed gray lines denote the PBL top height. For the tracer transport along the dashed arrows see text

same time (different from the situation in the CASES campaign over flat and very dry terrain in Figure 8). Since 0100 UTC corresponds to about 1900 LT (domain center), the current PBL top (derived from the Richardson number) is already lower than the highest altitudes that the tracer has reached by mixing at earlier times. The vertical range in between can be interpreted as the onset of the nighttime residual layer.

Of course, stronger mixing and mixing with higher altitudes causes a stronger downward momentum flux and, thus, more acceleration of the wind in the lowermost layer. In fact, in the tracer region, winds in the lowermost model layer are somewhat stronger with  $NLT_{3D}$  ( $\approx 5\text{--}9\text{ m}\cdot\text{s}^{-1}$ ), and weaker with the ACM2 and the MYNN scheme ( $4\text{--}8\text{ m}\cdot\text{s}^{-1}$ ). However, this does not fully explain the different motions of the tracer near the surface and by far not the very different vertical structure.

The vertical cross section in Figure 10 also exhibits a pronounced structure resembling a breaking water wave, at least for the simulations with  $NLT_{3D}$  and the ACM2 scheme: Obviously, tracer substance is mixed to higher altitudes with higher wind speeds and later (downstream) mixed back to lower altitudes and the ground (as sketched by the dotted arrows). So, mixing in a deeper PBL also means transport by stronger winds and an effectively faster horizontal transport of tracer even near the ground.

At 0600 UTC on the same day, about a third of the near-surface tracer air mass (with  $NLT_{3D}$  and ACM2) has already crossed the Appalachians (cf. dotted area in Figure 9). This holds for the simulations with  $NLT_{3D}$  and ACM2, which reasonably agree with the observations, whereas the tracer simulated with the MYNN scheme significantly lags behind.

At 1600 UTC, the tracer air mass in the simulations with  $NLT_{3D}$  and ACM2 has passed the Appalachians, in qualitative agreement with the observations, with the air mass in ACM2 traveling somewhat faster, as its eastern part has already completely crossed the coastline whereas tracer is still observed by coastal stations. However, the simulation with the MYNN scheme only shows an extension of the tracer air mass crossing the mountain ridge too far in the south, whereas the maximum of the tracer volume is still to follow.

During cases 4 and 5, after the passage of a cold front of a low north of Lake Ontario further moving to the northeast, the winds are predominantly northwesterly to northerly. This time the tracer was emitted from Sudbury at night. Nevertheless, the PBL was well mixed due to the passage of the cold front. In case 4, for example, on October 26, 1983, 1200 UTC after the release on October 26, 1983, 0345–0645 UTC, the tracer first moves southeastwards in all three simulations (i.e., all three PBL schemes,

see Figure 11) and starts to cross Lake Ontario, in good accordance with the observations, except in the simulation with the MYNN scheme, where the leading tracer edge is slightly behind.

At 2000 UTC, the tracer air mass has already crossed the St. Lawrence River in the simulations with  $NLT_{3D}$  and ACM2, although the observations suggest that the air mass should only stretch and extend to the area south of the river. This time the situation is best captured by the MYNN scheme with only about half of the tracer (in the lowermost model layer) having crossed the river.

However, finally on October 27, 1200 UTC, the tracer with both  $NLT_{3D}$  and ACM2 has crossed the Appalachians and reached the Atlantic Ocean in accordance with the observations, and with the MYNN scheme the tracer is mainly situated over the Appalachians. Compared with ACM2, the tracer air mass simulated with the  $NLT_{3D}$  scheme extends more to the south, as also suggested by the observations (at least over land). What all schemes miss here is to leave some amount of tracer scattered along the trajectory of the air mass. This is the main qualitative difference from the first three cases, where the tracer air mass moved as a whole, whereas here smaller portions are split off and left behind, or possibly re-emitted from the surface.

#### 4.2.2 | Fraction skill score

To evaluate these results in a more quantitative manner, we apply a fraction skill score (FSS) analysis, which is a scale-selective verification method (Roberts, 2008; Roberts and Lean, 2008). The tracer partial density is converted to a binary event (tracer/no tracer) by applying a threshold value. To allow for a more detailed analysis, we apply two thresholds:  $\rho_{th1}=0.0156\text{ ng}\cdot\text{m}^{-3}$  (detection limit) and a value one order of magnitude greater,  $\rho_{th2}=0.1\text{ ng}\cdot\text{m}^{-3}$ . We also checked  $\rho_{th3}=1$  and  $10\text{ ng}\cdot\text{m}^{-3}$ , but as these values are exceeded only in very small core volumes of the tracer air mass, all schemes produce very low FSS values (not shown), so that a comparison is not informative.

For each full hour in the simulation, the following procedure is applied: Starting from the observed partial densities  $\rho_k^{\text{obs}}$  ( $k$  over active stations only) and the simulation results  $\rho_{i,j}^{f,s}$  for the three schemes  $s$ , the above threshold criteria ( $th1, th2$ ) lead to two observed and six simulated binary datasets  $b_{k,th1,2}^{\text{obs}}$  and  $b_{i,j,th1,2}^{f,s}$  per case.

Averaging of the forecast binary events within a local environment ( $i_k - n, \dots, i_k + n; j_k - n, \dots, j_k + n$ ) around each grid point ( $i_k, j_k$ ) containing the location of an active station  $k$  and all active stations within a corresponding search radius of  $r = \Delta x (\frac{1}{2} + n)$  relative to the local station  $k$  results in tracer probabilities  $p_{i_k,j_k}^f$  and  $p_k^o$  for each forecast and the observation and for each threshold criterion. For

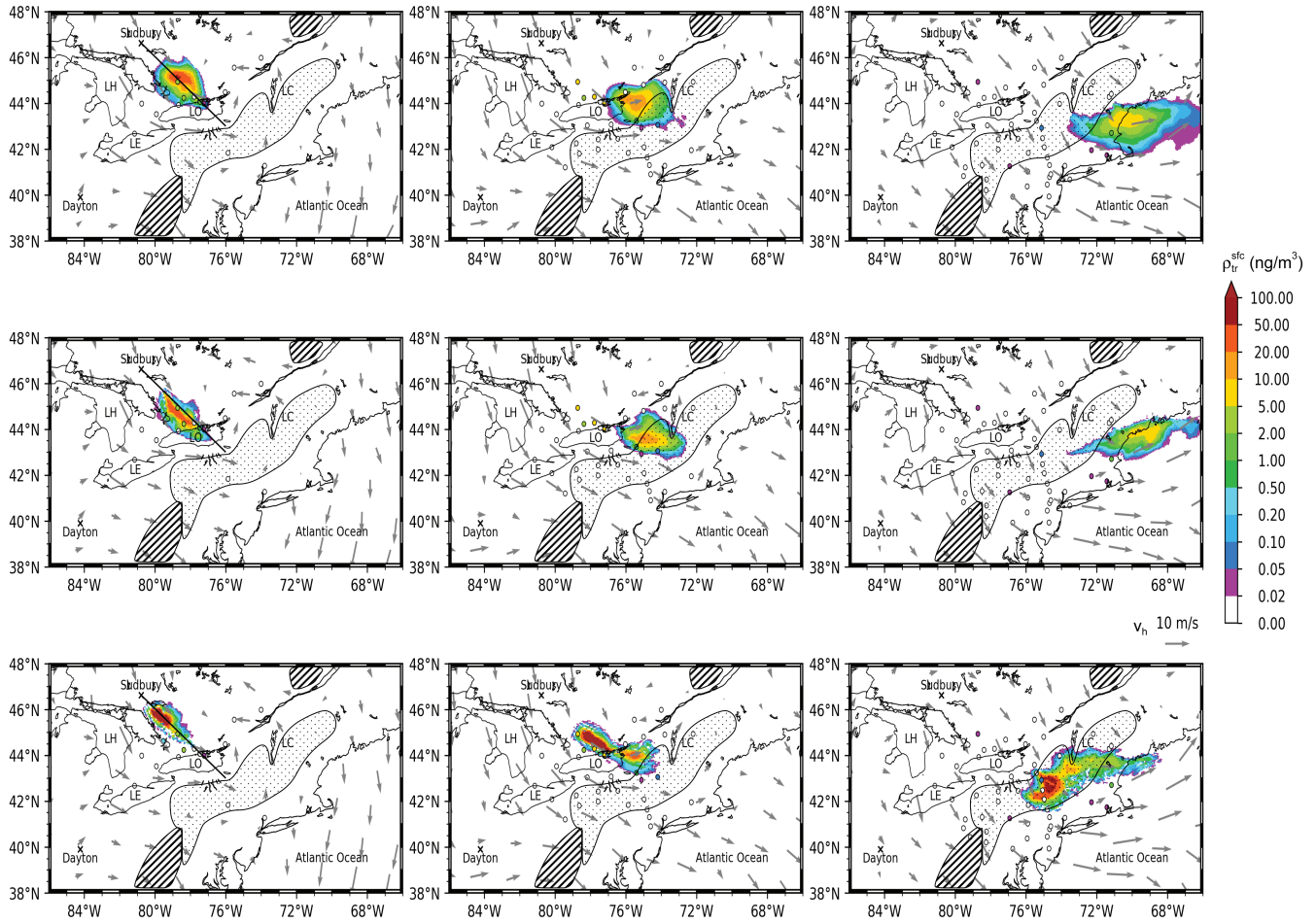


**FIGURE 11** As Figure 9, but during case 4 on October 26, 1983, 1200 (left column), 2000 (center column) and October 27, 1983, 1200 UTC (right column) simulated with WRF and the NLT<sub>3D</sub> (top row), ACM2 (center row), and MYNN scheme (bottom row)

the search radius  $r$  and the corresponding number of grid boxes, we choose  $n = 18$  ( $r = 103$  km), which is somewhat more than the typical distance between two observation stations, and  $n = 8$  ( $r = 47$  km). For  $n_a$  active stations, the fraction skill score (FSS) is then defined by the fraction Brier score (FBS) as

$$FBS = \frac{1}{n_a} \sum_{k=1}^{n_a} (p_{i_k, j_k}^f - p_k^o)^2$$

$$FBS_{\text{worst}} = \frac{1}{n_a} \sum_{k=1}^{n_a} (p_{i_k, j_k}^f)^2 + (p_k^o)^2$$

$$FSS = 1 - \frac{FBS}{FBS_{\text{worst}}} \quad (31)$$

$FBS_{\text{worst}}$  is the worst-case FBS and normalizes the FSS to the interval  $[0, 1]$  (Nachamkin and Schmidt, 2015). Values of  $FSS \geq 0.5$  denote a displacement error (between model and observation) smaller than half the FSS neighborhood size  $r = \Delta x (\frac{1}{2} + n)$ , so that the simulation then

has enough skill to be called “useful” at that spatial scale  $r$  (Roberts, 2008; Roberts and Lean, 2008).

Concerning the large-scale flow pattern and the performance of the PBL schemes, the five cases can be assigned to two classes, with case 3 and 4 as typical representatives. We start with initial southwesterly winds (cases 1–3) and the lower threshold value  $\rho_{th1} = 0.0156 \text{ ng} \cdot \text{m}^{-3}$ , which geometrically denotes the detectable boundary of the tracer air mass (Figure 12). The FSS time series reflect the qualitative results from the map inspections. Results from NLT<sub>3D</sub> and ACM2 are “useful” ( $FSS > 0.5$ ) for about half of the simulation time or even more, on all analyzed scales, that is, search radii. Often, especially in the middle part of the simulation, the FSS from NLT<sub>3D</sub> is comparable to or even somewhat higher than that from ACM2 on the corresponding scales. At both the start and end of the simulation, the observed tracer air mass is harder to catch by the simulation. At the start, the tracer air mass is still small and the FSS depends on the coincidence of the simulated tracer area with a few station locations. Towards the end of the



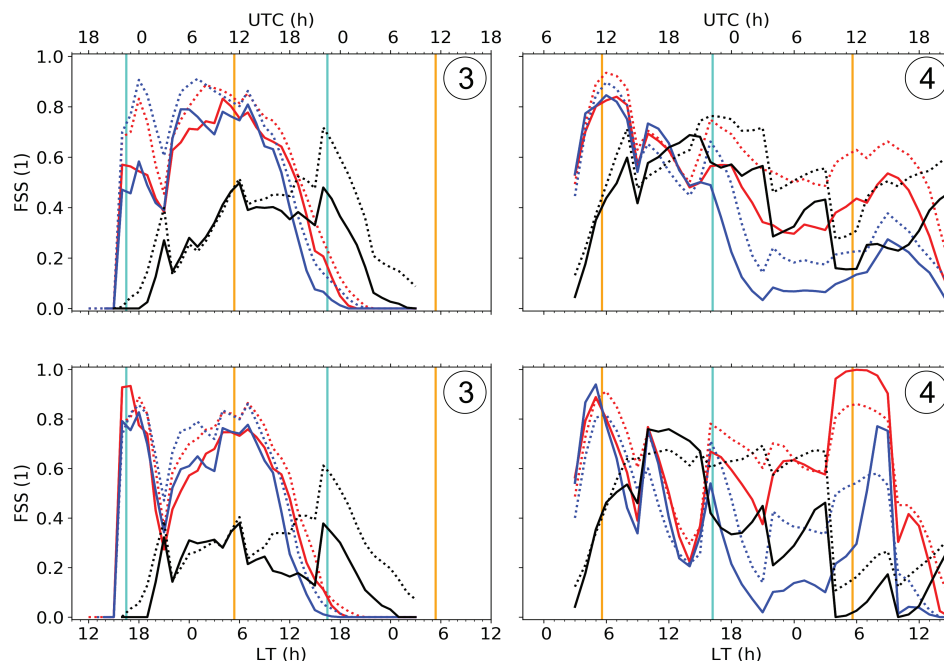


**FIGURE 12** FSS time series applying a threshold of  $\rho_{th}=0.0156 \text{ ng}\cdot\text{m}^{-3}$  (top row) and  $\rho_{th}=0.1 \text{ ng}\cdot\text{m}^{-3}$  (bottom row) for CAPTEX cases 3 (left column) and 4 (right column) as simulated with WRF including  $\text{NLT}_{3D}$  (red), ACM2 (blue), and the MYNN scheme (black) for search radii of 47 km (solid) and 103 km (dotted). Vertical lines denote the sunrise (orange) and sunset (light blue) at the simulation domain center

simulation, all deviations have summed up and forecast quality generally becomes poorer.

The simulations with the MYNN scheme often show lower FSS values and even  $\text{FSS} < 0.5$  for longer time periods, mainly because of the slower tracer transport described above. This also holds for the higher threshold value  $\rho_{th2}=0.1 \text{ ng}\cdot\text{m}^{-3}$ , where again  $\text{NLT}_{3D}$  and ACM2 compete with each other and the MYNN scheme exhibits the lowest FSS values. This is mostly because of the weaker vertical mixing in MYNN which hinders the tracer from being mixed into the higher PBL where stronger winds support the fast horizontal transport as in the observations. Since both of the vertically nonlocal schemes  $\text{NLT}_{3D}$  and ACM2 perform better than MYNN, the fast nonlocal upward mixing in contrary to the slower classical eddy mixing appears as the probable underlying process.

In cases 4 and 5, the initial FSS situation looks similar to above, but then after about local noon (case 4) or sunset (case 5), the simulations with  $\text{NLT}_{3D}$  and MYNN show the highest FSS values, whereas the results from ACM2 produce the lowest FSS. This corresponds to the findings from the map comparisons above (Figure 11), where the tracer transport by ACM2 is too fast compared with the observations. In case 5, all simulations have the tendency to produce lower FSS values, even below 0.5 (not shown).

To present the performance of the three PBL schemes for all cases in a compact form, we have averaged the FSS series in time and sorted the average FSS values in Table 3. We start with the cases with southwesterly winds. In cases 1 and 2,  $\text{NLT}_{3D}$  and ACM2 produce similar FSS values with  $\text{NLT}_{3D}$  partially showing slightly poorer performance. Both schemes, however, exhibit FSS values of

about 0.15–0.3 higher than the MYNN scheme. In case 3,  $\text{NLT}_{3D}$  produces slightly higher FSS values than ACM2, but the difference of both schemes compared with MYNN remains the same. The MYNN scheme often exhibits FSS values below 0.5, that is, the limit of “usefulness”. Among the cases with northwesterly winds, the picture is less uniform. In case 4,  $\text{NLT}_{3D}$  shows the highest FSS values, followed by MYNN and ACM2 with the lowest FSS. In case 5, ACM2 is the leading scheme in terms of averaged FSS, followed by  $\text{NLT}_{3D}$  and MYNN, which exhibits the lowest FSS.

The low FSS values for MYNN are mainly caused by its lack of strong and high-reaching nonlocal updrafts: As a detailed analysis of vertical cross sections from the tracer source downstream across the tracer air mass (not shown) reveals, especially in case 2 and 3, MYNN lifts the tracer to only 150 m above the surface after about 9 hrs. This is much lower than  $\text{NLT}_{3D}$  and ACM2, and it is far too low to reach the stronger winds in the upper PBL. Even in cases 1, 4, and 5, where MYNN lifts the tracer to 300–500 m above ground level, tracer concentrations aloft are much lower than with  $\text{NLT}_{3D}$  and ACM2 due to the step-by-step local mixing with dilution of the tracer at each step. Although the exact trajectories of the tracer parcels depend on many details when which part of the wind field is encountered, it is interesting to find that the highest FSS value for MYNN is obtained for case 1, which is just the case where the tracer is lifted to the highest altitude (500 m a.g.l.) by MYNN.

In total, when averaging the FSS over all five cases,  $\text{NLT}_{3D}$  and ACM exhibit similar results that are significantly higher than FSS values from MYNN. This suggests

**TABLE 3** Temporally averaged FSS values of the three PBL schemes for each case analyzed during the CAPTEX campaign (1983) and averaged FSS over all five cases (bottom block)

Case	$\rho_{th}$ $R$	0.0156 ng·m <sup>-3</sup>		0.1 ng·m <sup>-3</sup>	
		47 km	103 km	47 km	103 km
1	NLT <sub>3D</sub>	0.719	0.739	0.535	0.571
1	NLT <sub>1D</sub>	0.710	0.724	0.535	0.567
1	ACM2	0.745	0.749	0.656	0.678
1	MYNN	0.584	0.603	0.496	0.531
2	NLT <sub>3D</sub>	0.537	0.594	0.452	0.514
2	NLT <sub>1D</sub>	0.530	0.601	0.467	0.512
2	ACM2	0.547	0.611	0.456	0.510
2	MYNN	0.218	0.246	0.177	0.193
3	NLT <sub>3D</sub>	0.398	0.446	0.380	0.412
3	NLT <sub>1D</sub>	0.373	0.423	0.372	0.397
3	ACM2	0.365	0.438	0.353	0.407
3	MYNN	0.239	0.326	0.179	0.283
4	NLT <sub>3D</sub>	0.486	0.611	0.584	0.621
4	NLT <sub>1D</sub>	0.403	0.520	0.517	0.544
4	ACM2	0.332	0.404	0.325	0.407
4	MYNN	0.410	0.533	0.331	0.460
5	NLT <sub>3D</sub>	0.485	0.480	0.418	0.469
5	NLT <sub>1D</sub>	0.516	0.467	0.364	0.375
5	ACM2	0.620	0.543	0.625	0.550
5	MYNN	0.435	0.454	0.381	0.384
all	NLT <sub>3D</sub>	0.525	0.574	0.474	0.517
all	NLT <sub>1D</sub>	0.506	0.547	0.451	0.479
all	ACM2	0.522	0.549	0.483	0.510
all	MYNN	0.377	0.432	0.313	0.370

Note:  $R$  and  $\rho_{th}$  denote the search radii and tracer concentration threshold.

that vertically nonlocal schemes are superior to local turbulence schemes. To better characterize the difference between NLT<sub>3D</sub> and ACM2, more comparison cases and more tuning compared with established schemes may be necessary.

### 4.3 | Three-dimensional turbulence

To demonstrate the effect of three-dimensional turbulence, we employ a version of the NLT<sub>3D</sub> scheme with the horizontal mixing switched off, denoted by NLT<sub>1D</sub>. Instead, WRF's standard horizontal Smagorinsky first-order diffusion is applied, as recommended in the WRF user guide (Wang *et al.*, 2019).

First, we analyze the effect of horizontal turbulence in the NLT<sub>3D</sub> scheme for the CASES-99 simulations at

higher resolutions ( $\Delta x = 1.7$  km, 600 m). As already shown in Figure 8 for  $\Delta x = 5$  km, the larger cities in the model domain show up as areas of deeper PBL in the evening. This is because they represent heat islands maintaining PBL convection for several hours after sunset (cf. Figure 13).

As Figure 13 (left column) reveals for the case of Wichita, which is included in all three model nests, the area of deeper PBL is more extended for NLT<sub>3D</sub> than for NLT<sub>1D</sub> due to the horizontal turbulent activity. As  $\theta_v$  profiles (not shown) from the city area compared with the country side show, this deeper PBL is accompanied by somewhat higher air temperatures near the ground. However, the cause of the deeper PBL is the absence of a weak inversion quickly forming over the lowermost model layer outside the city area. Thus, the City of Wichita does show up as a heat island with temperatures about 3 K warmer



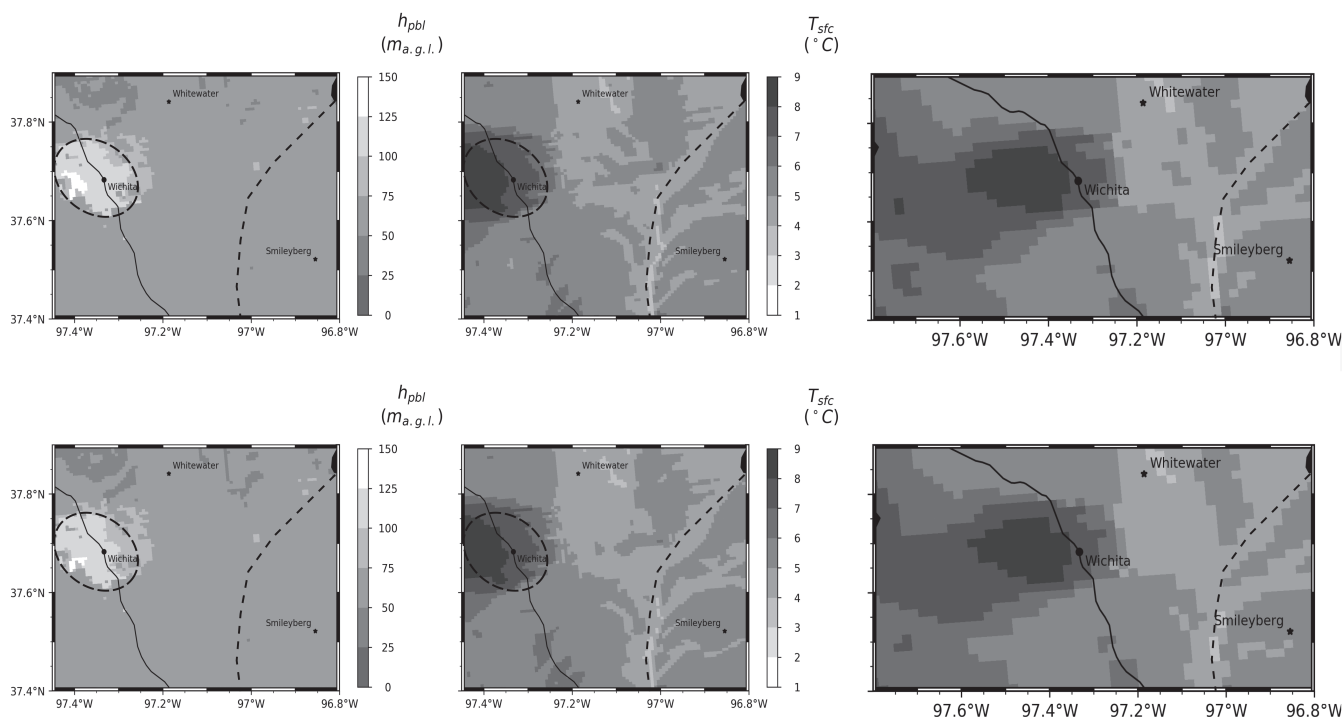


**FIGURE 13** Simulation WRF including the  $NLT_{3D}$  scheme (top row) and the one-dimensional (vertical)  $NLT_{1D}$  scheme combined with a standard horizontal Smagorinsky diffusion (bottom row) on October 24, 1999, 0600 UTC (0000 LT). Left column: PBL depth in the innermost nest with  $\Delta x = 600$  m. Center column: air temperature of the lowermost model layer in the innermost nest ( $\Delta x = 600$  m). Right column: as center column but for the medium-resolution nest ( $\Delta x = 1.7$  km), same color code as for the center column. In order not to cover small temperature structures, the Walnut River is drawn as a dashed line. For orientation, the solid ellipse denotes the area of elevated  $h_{PBL}$  as taken from the upper left map

than the environment, but the effect of horizontal turbulence here is difficult to see in the near-surface air temperatures. Because of the easterly winds, the horizontal mixing effect is somewhat more visible west of Wichita, where the warm urban air is mixed farther downstream with  $NLT_{3D}$  than with  $NLT_{1D}$  (cf. Figure 13, right column).

The structures of near-surface air temperature east of Wichita are mainly caused by the shallow valleys of the Walnut River and its feeders. In the simulations with both  $\Delta x = 1.7$  km and  $\Delta x = 600$  m with  $NLT_{3D}$  including horizontal turbulence, temperatures are somewhat higher than with  $NLT_{1D}$ . Since the soil is already cooling for several hours and turbulence here is suppressed (cf. PBL depths in Figure 13, left column), this warmer air must be a remnant from the stronger mixing before sunset.

Some effects of the horizontal turbulence also show up at larger grid sizes ( $\Delta x = 5$  km) as used for the tracer studies of CAPTEX. Figure 14 compares simulations from case 4 with  $NLT_{3D}$  and  $NLT_{1D}$  on October 26, 1983, 0600 LT, about one day and one night after the tracer release at Sudbury. The prevailing northwesterly winds have advected the tracer air mass over a relatively flat terrain, and turbulence has broadened the tracer air mass perpendicular to the direction of advection (approx. solid line in Figure 14,

left). The edge of the tracer air mass looks smoother for the simulation with  $NLT_{3D}$  than with  $NLT_{1D}$  and somewhat broader for  $NLT_{3D}$ , but this actually depends on exactly where to place the cross section. The cross section perpendicular to the direction of advection from  $NLT_{1D}$  clearly shows the effect of fast nonlocal mixing during the last day: Subsequently, the red and orange contours exhibit a small anvil-like structure caused by the deposition of tracer in the upper PBL. For  $NLT_{3D}$ , the anvil top is only slightly broader, but its updraft region in the lower and middle PBL is much wider as an effect of the stronger horizontal mixing in  $NLT_{3D}$ . This facilitates the lifting of near-surface air towards the PBL top, where advection is accelerated by the stronger grid-scale winds. This can be seen in the cross section parallel to the direction of advection (dotted line in Figure 14, left): following the orange and yellow contours reveals a much more massive advance of the tracer air mass for  $NLT_{3D}$  than for  $NLT_{1D}$ .

As Table 3 reveals, simulations with  $NLT_{3D}$  produce equal or higher FSS values in 17 out of 20 comparisons with  $NLT_{1D}$  including horizontal Smagorinsky diffusion. This is in accordance with the FSS averaged over all cases, where  $NLT_{3D}$  is always superior to  $NLT_{1D}$  with horizontal Smagorinsky diffusion. In summary, this demonstrates a

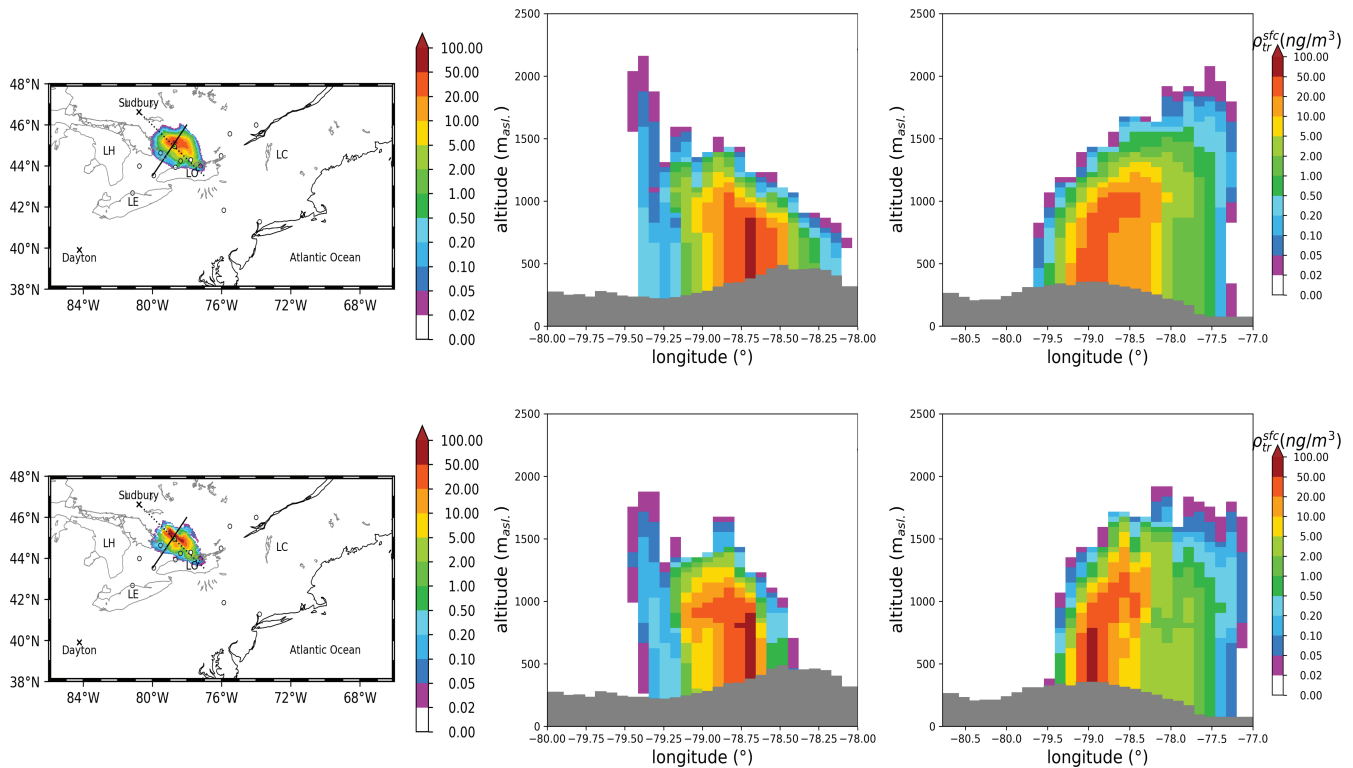


**FIGURE 14** Effects of horizontal turbulence in the  $NLT_{3D}$  scheme as demonstrated by a comparison of simulations with the full three-dimensional  $NLT_{3D}$  scheme (top row) and one-dimensional (vertical)  $NLT_{1D}$  scheme combined with a standard horizontal Smagorinsky diffusion, both during case 4 on October 26, 1983, 1200 UTC (0600 LT). Maps of the near-surface tracer distribution (left column), vertical cross sections perpendicular to the grid-scale winds (along the solid line in the map; center column), and parallel to the grid-scale winds (along the dotted line in the map; right column)

certain benefit from three-dimensional turbulence already at grid sizes of about 5 km.

## 5 | CONCLUSIONS

With increasing computer power and decreasing grid sizes, NWP modeling increasingly enters a gray zone where classical subgrid phenomena become at least partially resolved. So, in contemporary NWP models, turbulence is already partially resolved in the vertical (at least for the biggest PBL eddies). This has led to the development of (vertically) nonlocal PBL schemes. With horizontal grid sizes approaching a few kilometers or smaller, turbulence will soon also become horizontally partially resolved, so that a 3D and possibly also horizontally nonlocal formulation of the PBL scheme will have to be considered.

A very flexible formulation of nonlocal turbulence is the so-called transilient matrix formalism by Stull (1984); Stull and Hasegawa (1984) that has been used in several state-of-the-art PBL schemes, as, for example, ACM2 (Pleim, 2007a; 2007b). Based on this matrix formalism, we have developed the  $NLT_{3D}$  turbulence scheme. To enable possible horizontal turbulent mixing in future

finely resolved hosting models, the  $NLT_{3D}$  scheme applies mixing matrices to subgrid-scale transports in all three dimensions. At the current stage,  $NLT_{3D}$  includes local horizontal mixing, that is, between directly neighboring grid columns, but it could easily be extended to nonlocal horizontal mixing. From the horizontal extent of the involved eddies and the grid size, the scheme determines which of the off-diagonal elements will be nonzero. Their magnitude can be derived from the turbulent activity (similar to the present procedure for local horizontal mixing) and the fraction of subgrid motion (cf. Honnert *et al.*, 2011).

We have tested the  $NLT_{3D}$  scheme with WRF simulations of real cases, the results of which are compared with observational data from corresponding field campaigns. Furthermore, we also compared with WRF simulations including the local MYNN scheme as a classical local turbulence scheme and the ACM2 scheme as a one-dimensional nonlocal transilient scheme.

For the simulations from the CASES-99 campaign over homogeneous terrain (North American prairie, flat orography, grassland) all three turbulence schemes perform well and very similarly. They generally reproduce the observations from EBBR surface flux stations and radiosonde

profiles, although the surface fluxes are slightly underestimated and atmospheric moisture and momentum provide hints of a somewhat too weak interaction with the surface. Single horizontal temperature inhomogeneities such as urban heat islands and shallow river basins offer the opportunity to analyze the effect of horizontal turbulent mixing in the NLT<sub>3D</sub> scheme. For that purpose, NLT<sub>3D</sub> and a “one-dimensional” version NLT<sub>1D</sub> where horizontal turbulence has been replaced by standard horizontal Smagorinsky diffusion, are compared. With NLT<sub>3D</sub>, warm surface air extends farther downstream of urban heat islands and shallow river basins stay warmer in the evening than with NLT<sub>1D</sub>. The evening PBL top stays high over a larger area over urban areas with NLT<sub>3D</sub> compared with NLT<sub>1D</sub>. Averaged over the whole model domain, the PBL depth exhibits similar diurnal cycles for NLT<sub>3D</sub> and ACM2, whereas with MYNN with its TKE-dependent mixing the PBL decays very slowly in the evening and night.

Simulations over complex terrain during the CAPTEX campaign (Appalachian mountains, medium-altitude structured orography, inhomogeneous vegetation) reveal more differences between the three turbulence schemes. Problems of the MYNN scheme concerning the tracer transport, which is simulated too slow near the surface, can be traced back to a too shallow PBL. Simulations with the NLT<sub>3D</sub> and ACM2 schemes produce much deeper convective PBL and, thus, mix more momentum down to the surface and more tracer up to higher altitudes, where stronger winds prevail. Additionally, as vertical cross sections reveal, the tracer air mass is tilted downstream and fast-moving tracer from higher altitudes is mixed back to the ground. Both effects, which are strongest with the NLT<sub>3D</sub> scheme, lead to a faster tracer transport, which better agrees with the near-surface tracer observations. Comparisons with NLT<sub>1D</sub> reveal that nonlocal updraft regions are broadened by horizontal turbulence lifting tracer-marked surface air more effectively to the upper PBL. The inclusion of horizontal turbulence in NLT<sub>3D</sub> is also beneficial for the FSS. For most analyzed CAPTEX cases, NLT<sub>3D</sub> produces similar and partially higher FSS values compared with ACM2. Due to its lack of strong non-local updrafts, MYNN usually produces the lowest FSS.

These first promising results obtained from NLT<sub>3D</sub> can mainly be attributed to the inclusion of horizontal turbulence, which is not only important at small grid sizes ( $\Delta x = 1.7$  km and 600 m) but shows its first effects already at  $\Delta x = 5$  km.

## AUTHOR CONTRIBUTIONS

**V. Kuell:** conceptualization; data curation; formal analysis; investigation; methodology; validation; visualization;

writing – original draft; writing – review and editing. **A. Bott:** conceptualization; formal analysis; funding acquisition; methodology; project administration; resources; supervision; writing – original draft; writing – review and editing.

## ACKNOWLEDGEMENTS

The authors gratefully acknowledge the National Center for Atmospheric Research (NCAR) and the University Corporation for Atmospheric Research (UCAR) for providing the WRF model and the NOAA Air Resources Laboratory (ARL) for the provision of the Data Archive of Tracer Experiments and Meteorology (DATEM) used in this publication. The Argonne National Laboratory (ANL) and its Atmospheric Boundary Layer Experiments (ABLE) Facility as well as the Earth Observing Laboratory (EOL) of NCAR/UCAR are acknowledged for providing observational data of the CASES-99 campaign. The European Centre for Medium-Range Weather Forecasts (ECMWF) is acknowledged for providing ERA5 reanalysis data (ERA5 hourly data on pressure levels and single levels from 1979 to present) via the Copernicus Climate Change Service (C3S) Climate Data Store (CDS). We gratefully acknowledge the helpful and constructive comments of the reviewers of the paper. Our work was funded by the Deutsche Forschungsgemeinschaft (DFG grant Bo 998/18-1).

## ORCID

V. Kuell  <https://orcid.org/0000-0001-6012-1697>

A. Bott  <https://orcid.org/0000-0001-9747-9406>

## REFERENCES

- Ansmann, A., Fruntke, J. and Engelmann, R. (2010) Updraft and downdraft characterization with Doppler lidar: cloud-free versus cumuli-topped mixed layer. *Atmospheric Chemistry and Physics*, 10, 7845–7858.
- Beare, R.J., MacVean, M.K., Holtslag, A.A.M., Cuxart, J., Esau, I., Golaz, J.-C., Jimenez, M.A., Khairoutdinov, M., Kosovic, B., Lewellen, D., Lund, T.S., Lundquist, J.K., McCabe, A., Moene, A.F., Noh, Y., Raasch, S. and Sullivan, P. (2006) An intercomparison of large-eddy simulations of the stable boundary layer. *Boundary-Layer Meteorology*, 118, 247–272.
- Blackadar, A.K. (1979). Modeling pollutant transfer during daytime convection, *Fourth Symposium on Atmospheric Turbulence, Diffusion, and Air Quality*, pp. 443–447. Boston, MA: American Meteorological Society.
- Blackadar, A.K. (1962) The vertical distribution of wind and turbulent exchange in a neutral atmosphere. *Journal of Geophysical Research*, 67(D08), 3095–3102.
- Bosveld, F.C., Baas, P., van Meijgaard, E., de Bruijn, E.I.F., Steeneveld, G.-J. and Holtslag, A.A.M. (2014) The third GABLS intercomparison case for evaluation studies of boundary-layer models. Part A: case selection and set-up. *Boundary-Layer Meteorology*, 152, 133–156.

- Chou, M.D. and Suarez, M.J. (1999). A solar radiation parameterization for atmospheric studies. NASA Technical Memorandum 104606.
- Chou, M.D. and Suarez, M.J. (2001). A thermal infrared radiation parameterization for atmospheric studies. NASA Technical Memorandum 104606.
- Cuxart, J., Holtslag, A.A.M., Beare, R.J., Bazile, E., Beljaars, A., Cheng, A., Conangla, L., Ek, M., Freedman, F., Hamdi, R., Kerstein, A., Kitagawa, H., Lenderink, G., Lewellen, D., Mailhot, J., Mauritsen, T., Perov, V., Schayes, G., Steeneveld, G.-J., Svensson, G., Taylor, P., Weng, W., Wunsch, S. and Xu, K.-M. (2006) Single-column model intercomparison for a stably stratified atmospheric boundary layer. *Boundary-Layer Meteorology*, 118, 273–303.
- Deardorff, J.W. (1966) The counter-gradient heat flux in the lower atmosphere and in the laboratory. *Journal of the Atmospheric Sciences*, 23, 503–506.
- Ebert, E.E., Schumann, U. and Stull, R.B. (1989) Nonlocal turbulent mixing in the convective boundary layer evaluated from large eddy simulation. *Journal of the Atmospheric Sciences*, 46, 2178–2207.
- Ferber, G.J., Heffter, J.L., Draxler, R.R., Lagomarsino, R.J., Thomas, F.L., Dietz, R.N. and Benkovitz, C.M. (1986). Cross-Appalachian Tracer Experiment (CAPTEX '83) final report.
- Fiedler, B.H. (1984) An integral closure model for the vertical turbulent flux of a scalar in a mixed layer. *Journal of the Atmospheric Sciences*, 41, 674–680.
- Fiedler, B.H. and Moeng, C.-H. (1985) A practical integral closure model for mean vertical transport of a scalar in a convective boundary layer. *Journal of the Atmospheric Sciences*, 42, 359–363.
- Foken, T. (2006) *Angewandte Meteorologie* (2nd edition). New York, NY: Springer.
- Forster, C. and Stohl, A. (2007) Parameterization of convective transport in a Lagrangian particle dispersion model and its evaluation. *Journal of Applied Meteorology*, 46, 403–422.
- Hersbach, H., Bell, B., Berrisford, P., Hirahara, S., Horanyi, A., Muñoz-Sabater, J., Nicolas, J., Peubey, C., Radu, R., Schepers, D., Simmons, A., Soci, C., Abdalla, S., Abellan, X., Balsamo, G., Bechtold, P., Biavati, G., Bidlot, J., Bonavita, M., De Chiara, G., Dahlgren, P., Dee, D., Diamantakis, M., Dragani, R., Flemming, J., Forbes, R., Fuentes, M., Geer, A., Haimberger, L., Healy, S., Hogan, R.J., Holm, E., Janiskova, M., Keeley, S., Laloyaux, P., Lopez, P., Lupu, C., Radnoti, G., de Rosnay, P., Rozum, I., Vamborg, F., Villaume, S. and Thepaut, J.-N. (2020) The ERA5 global reanalysis. *Quarterly Journal of the Royal Meteorological Society*, 146, 1999–2049.
- Holtslag, A.A.M., Svensson, G., Baas, P., Basu, S., Beare, B., Beljaars, A.C.M., Bosveld, F.C., Cuxart, J., Lindvall, J., Steeneveld, G.J., Tjernström, M. and Van De Wiel, B.J.H. (2013) Stable atmospheric boundary layers and diurnal cycles: challenges for weather and climate models. *Bulletin of the American Meteorological Society*, 94, 1691–1706.
- Hong, S.-Y., Noh, Y. and Dudhia, J. (2006) A new vertical diffusion package with an explicit treatment of entrainment processes. *Monthly Weather Review*, 134, 2318–2341.
- Honnert, R., Masson, V. and Couvreux, F. (2011) A diagnostic for evaluating the representation of turbulence in atmospheric models at the kilometer scale. *Journal of the Atmospheric Sciences*, 68, 3112–3131.
- Inclan, M.G., Forkel, R., Dlugi, R. and Stull, R.B. (1996) Application of transilient turbulent theory to study interactions between the atmospheric boundary layer and forest canopies. *Boundary-Layer Meteorology*, 79, 315–344.
- Jimenez, P.A., Dudhia, J., Gonzalez-Rouco, J.F., Navarro, J., Montavez, J.P. and Garcia-Bustamente, E. (2012) A revised scheme for the WRF surface layer formulation. *Monthly Weather Review*, 140, 898–918.
- Laprise, R. (1992) The euler equations of motion with hydrostatic pressure as an independent variable. *Monthly Weather Review*, 120, 197–207.
- Lareau, N.P., Zhang, Y. and Klein, S.A. (2018) Observed boundary layer controls on shallow cumulus at the ARM Southern Great Plains Site. *Journal of the Atmospheric Sciences*, 75, 2235–2255.
- LeMone, M.A., Grossman, R.L., Coulter, R.L., Wesley, M.L., Klazura, G.E., Poulos, G.S., Blumen, W., Lundquist, J.K., Cuenca, R.H., Kelly, S.F., Brandes, E.A., Oncley, S.P., McMillen, R.T. and Hicks, B.B. (2000) Land-atmosphere interaction research, early results, and opportunities in the Walnut River watershed in southeast Kansas: CASES and ABLE. *Bulletin of the American Meteorological Society*, 81, 757–779.
- LeMone, M.A., Grossman, R.L., McMillen, R.T., Liou, K.-N., Ou, S.C., McKeen, S., Angevine, W., Ikeda, K. and Chen, F. (2002) CASES-97: late-morning warming and moistening of the convective boundary layer over the Walnut River watershed. *Boundary-Layer Meteorology*, 104, 1–52.
- Louis, J.-F. (1979) A parametric model of vertical eddy fluxes in the atmosphere. *Boundary-Layer Meteorology*, 17, 187–202.
- Mellor, G.L. and Yamada, T. (1982) Development of a turbulence closure model for geophysical fluid problems. *Reviews of Geophysics and Space Physics*, 20, 851–875.
- Nachamkin, J.E. and Schmidt, J. (2015) Applying a neighborhood fractions sampling approach as a diagnostic tool. *Monthly Weather Review*, 143, 4736–4749.
- Nakanishi, M. and Niino, H. (2006) An improved Mellor–Yamada level 3 model: its numerical stability and application to a regional prediction of advecting fog. *Boundary-Layer Meteorology*, 119, 397–407.
- Nakanishi, M. and Niino, H. (2009) Development of an improved turbulence closure model for the atmospheric boundary layer. *Journal of the Meteorological Society of Japan*, 87, 895–912.
- Ni, W.G. (1997) A coupled transilience model for turbulent air flow within plant canopies and the planetary boundary layer. *Agricultural and Forest Meteorology*, 86, 77–105.
- Olson, J.B., Kenyon, J.S., Angevine, W.M., Brown, J.M., Pagowski, M. and Suselj, K. (2019). A description of the MYNN-EDMF scheme and the coupling to other components in WRF–ARW. NOAA Technical Memorandum OAR GSD 61.
- Pleim, J.E. (2007a) A combined local and nonlocal closure model for the atmospheric boundary layer. Part I: model description and testing. *Journal of Applied Meteorology and Climatology*, 46, 1383–1395.
- Pleim, J.E. (2007b) A combined local and nonlocal closure model for the atmospheric boundary layer. Part II: application and evaluation in a mesoscale meteorological model. *Journal of Applied Meteorology and Climatology*, 46, 1396–1409.
- Pleim, J.E. and Chang, J.C. (1992) A non-local closure model for vertical mixing in the convective boundary layer. *Atmospheric Environment*, 26, 965–981.



- Poulos, G.S., Blumen, W., Fritts, D.C., Lundquist, J.K., Sun, J., Burns, S.P., Nappo, C., Banta, R., Newsom, R., Cuxart, J., Terradellas, E., Balsley, B. and Jensen, M. (2002) CASES-99: a comprehensive investigation of the stable nocturnal boundary layer. *Bulletin of the American Meteorological Society*, 83, 555–581.
- Raymond, W.H. and Stull, R.B. (1990) Application of transilient turbulence theory to mesoscale numerical weather forecasting. *Monthly Weather Review*, 118, 2471–2499.
- Roberts, N. (2008) Assessing the spatial and temporal variation in the skill of precipitation forecasts from an NWP model. *Meteorological Applications*, 15, 163–169.
- Roberts, N.M. and Lean, H.W. (2008) Scale-selective verification of rainfall accumulations from high-resolution forecasts of convective events. *Monthly Weather Review*, 136, 78–97.
- Romps, D.M. and Kuang, Z. (2011) A transilient matrix for moist convection. *Journal of the Atmospheric Sciences*, 68, 2009–2025.
- Schmidt, W. (1925) *Der Massenaustausch in freier Luft und verwandte Erscheinungen*. Hamburg: Henri Grand Verlag, Probleme der kosmischen Physik.
- Schumann, U. (1989) Large-eddy simulation of turbulent diffusion with chemical reactions in the convective boundary layer. *Atmospheric Environment*, 23, 1713–1727.
- Shin, H.H. and Hong, S.-Y. (2011) Intercomparison of planetary boundary-layer parametrizations in the WRF model for a single day from CASES-99. *Boundary-Layer Meteorology*, 139, 261–281.
- Skamarock, W.C., Klemp, J.B., Dudhia, J., Gill, D.O., Liu, Z., Berner, J., Wang, W., Powers, J.G., Duda, M.G., Barker, D.M. and Huang, X.-Y. (2019) *A description of the Advanced Research WRF Version 4*, (p. 145). Boulder, CO: National Center of Atmospheric Research, NCAR. NCAR Technical Note NCAR/TN-556+STR.
- Smagorinsky, J. (1963) General circulation experiments with the primitive equations: I The basic equations. *Monthly Weather Review*, 91, 99–164.
- Soares, P.M.M., Miranda, P.M.A., Siebesma, A.P. and Teixeira, J. (2004) An eddy-diffusivity/mass-flux parametrization for dry and shallow cumulus convection. *Quarterly Journal of the Royal Meteorological Society*, 130, 3365–3383.
- Steenveld, G.-J., Mauritsen, T., De Bruijn, E.I.F., Vila-Guerau De Arellano, J., Svensson, G. and Holtslag, A.A.M. (2008) Evaluation of limited-area models for the representation of the diurnal cycle and contrasting nights in CASES-99. *Journal of Applied Meteorology and Climatology*, 47, 869–887.
- Stull, R.B. (1984) Transilient turbulence theory. Part I: the concept of eddy-mixing across finite distances. *Journal of the Atmospheric Sciences*, 41, 3351–3367.
- Stull, R.B. (1988) *An Introduction to Boundary Layer Meteorology*. Dordrecht, The Netherlands: Kluwer Academic Publishers.
- Stull, R.B. (1993) Review of non-local mixing in turbulent atmospheres: transilient turbulence theory. *Boundary-Layer Meteorology*, 62, 21–96.
- Stull, R.B. and Driedonks, A.G.M. (1987) Application of the transilient turbulence parameterization to atmospheric boundary-layer simulations. *Boundary-Layer Meteorology*, 40, 209–239.
- Stull, R.B. and Hasegawa, T. (1984) Transilient turbulence theory. Part II: turbulent adjustment. *Journal of the Atmospheric Sciences*, 41, 3368–3379.
- Svensson, G., Holtslag, A.A.M., Kumar, V., Mauritsen, T., Steeneveld, G.J., Angevine, W.M., Bazile, E., Beljaars, A., de Bruijn, E.I.F., Cheng, A., Conangla, L., Cuxart, J., Ek, M., Falk, M.J., Freedman, F., Kitagawa, H., Larson, V.E., Lock, A., Mailhot, J., Masson, V., Park, S., Pleim, J., Söderberg, S., Weng, W. and Zampieri, M. (2011) Evaluation of the diurnal cycle in the atmospheric boundary layer over land as represented by a variety of single-column models: the second GABLS experiment. *Boundary-Layer Meteorology*, 140, 177–206.
- Tao, W.-K., Simpson, J. and McCumber, M. (1989) An ice–water saturation adjustment. *Monthly Weather Review*, 117, 231–235.
- Tao, W.-K., Wu, D., Lang, S., Chern, J.-D., Peters-Lidard, C., Fridlind, A. and Matsui, T. (2016) High-resolution NU-WRF simulations of a deep convective-precipitation system during MC3E: further improvements and comparisons between Goddard microphysics schemes and observations. *Journal of Geophysical Research*, 121, 1278–1305.
- Teixeira, J. and Siebesma, A.P. (2000). A mass-flux/K diffusion approach to the parameterization of the convective boundary layer: global model results, *Proceedings of 14th AMS Symposium on Boundary Layers and Turbulence*, pp. 133–136. Aspen, CO: American Meteorological Society.
- Tewari, M., Chen, F., Wang, W., Dudhia, J., LeMone, M.A., Mitchell, K., Ek, M., Gayno, G., Wegiel, J. and Cuenca, R.H. (2004). Implementation and verification of the unified NOAA land surface model in the WRF model, *20th Conference on Weather Analysis and Forecasting/16th Conference on Numerical Weather Prediction*, (Vol. 1115, pp. 11–15). Seattle, WA: American Meteorological Society.
- Troen, I.B. and Mahrt, L. (1986) A simple model of the atmospheric boundary layer: sensitivity to surface evaporation. *Boundary-Layer Meteorology*, 37, 129–148.
- Wang, W., Bruyere, C., Duda, M., Dudhia, J., Gill, D., Kavulich, M., Werner, K., Chen, M., Lin, H.-C., Michalakes, J., Rizvi, S., Zhang, X., Berner, J., Munoz-Esparza, D., Reen, B., Ha, S., Fossell, K., Beezley, J.D., Coen, J.L. and Mandel, J. (2019) *User's Guide for the Advanced Research WRF (ARW) Modeling System Version 4.1*. Boulder, CO: Mesoscale and Microscale Meteorology Laboratory, National Center for Atmospheric Research. Available at: <https://www2.mmm.ucar.edu/wrf/users>
- Zdunkowski, W. and Bott, A. (2003) *Dynamics of the Atmosphere: A Course in Theoretical Meteorology*. Cambridge, UK: Cambridge University Press.
- Zhang, X., Bao, J.-W., Chen, B. and Grell, E.D. (2018) A three-dimensional scale-adaptive turbulent kinetic energy scheme in the WRF-ARW model. *Monthly Weather Review*, 146, 2023–2045.

**How to cite this article:** Kuell, V. & Bott, A. (2022) A nonlocal three-dimensional turbulence parameterization (NLT<sub>3D</sub>) for numerical weather prediction models. *Quarterly Journal of the Royal Meteorological Society*, 148(742), 117–140. Available from: <https://doi.org/10.1002/qj.4195>